Spatiotemporal Variability in the Vertical Distribution of Phytoplankton Biomass in the Ice-Free Southern Ocean: A Bioregionalization Approach

N. Mayot, J. Uitz, L. Lacour, R. Sauzède, L. Izard, D. Nerini

Global Biogeochemical Cycles

RESEARCH ARTICLE
10.1029/2025GB008930

Spatiotemporal Variability in the Vertical Distribution of Phytoplankton Biomass in the Ice-Free Southern Ocean: A Bioregionalization Approach

N. Mayot[1,2], J. Uitz[1], L. Lacour[1], R. Sauzède[3], L. Izard[4], and D. Nerini[5]

[1]Laboratoire d'Océanographie de Villefranche (LOV), CNRS, Sorbonne Université, Villefranche-sur-Mer, France, [2]Centre national d'études spatiales (CNES), Paris, France, [3]Institut de la Mer de Villefranche (IMEV), CNRS, Sorbonne Université, Villefranche-sur-mer, France, [4]Laboratoire Océanographie et Climat: Experiments and Numerical Approaches (LOCEAN), CNRS, IRD, MNHN, Sorbonne Université, Paris, France, [5]Mediterranean Institute of Oceanography (MIO), CNRS, IRD, Aix Marseille Université, Marseille, France

Key Points:

- Each year, ~43% of the Southern Ocean exhibits expected phytoplankton phenology, while the rest shows interannual or atypical variability
- The Subantarctic Front and a northward decrease in surface nitrate strongly shape Southern Ocean phytoplankton biogeography
- Southern Annular Mode might drive interannual biomass variability in subtropical waters, while stratification constrains subsurface biomass at high latitudes

Supporting Information:

Supporting Information may be found in the online version of this article.

Correspondence to:

N. Mayot,
nicolas.mayot@imev-mer.fr

Citation:

Mayot, N., Uitz, J., Lacour, L., Sauzède, R., Izard, L., & Nerini, D. (2026). Spatiotemporal variability in the vertical distribution of phytoplankton biomass in the ice-free Southern Ocean: A bioregionalization approach. *Global Biogeochemical Cycles*, *40*, e2025GB008930. https://doi.org/10.1029/2025GB008930

Received 12 OCT 2025
Accepted 28 MAR 2026

Abstract The Southern Ocean plays a major role in the global oceanic sink of carbon dioxide (CO_2). However, substantial uncertainties remain regarding how phytoplankton production influences this carbon sink. Observations of the spatiotemporal variability in vertical phytoplankton biomass distribution are therefore essential to advance our understanding of the Southern Ocean CO_2 sink. This study analyzes a 25-year (1998–2022) database of spatially gridded, weekly averaged, vertical profiles of chlorophyll-*a* concentration and particulate backscattering coefficients to characterize seasonal to inter-annual dynamics in phytoplankton biomass. A two-step Principal Component Analysis workflow was used to extract the dominant modes of vertical variability in the profiles and to characterize their seasonal dynamics. The resulting seasonal descriptors were then used as input to a Gaussian Mixture Model to delineate phytoplankton-based bioregions across the Southern Ocean. The bioregionalization was strongly shaped by iron limitation and the position of the Subantarctic Front. Each year, approximately 43% of the Southern Ocean exhibited expected annual cycles of vertical phytoplankton biomass, while the remaining regions were characterized by interannual variability or undefined phenological patterns. At high latitudes in summer, the regional detection of recurring subsurface phytoplankton biomass maxima might be constrained by stratification dynamics. In subtropical regions, interannual variability in spring phytoplankton biomass may be indirectly influenced by the Southern Annular Mode through its modulation of wintertime vertical mixing. This bioregionalization provides a spatial framework for further investigating biologically driven carbon fluxes in the Southern Ocean.

Plain Language Summary Phytoplankton, microscopic algae, play a key role in the ocean's ability to absorb carbon dioxide from the atmosphere. In the Southern Ocean, their growth and distribution vary greatly with depth, season, and climate conditions. Using a 25-year observation-based database, we investigated how phytoplankton biomass changes vertically and seasonally across the Southern Ocean. We applied statistical clustering methods to identify regions with similar patterns of phytoplankton variability. Our analysis revealed six major bioregions that group into three broad zones: subtropical, subantarctic, and antarctic. About 43% of the Southern Ocean shows consistent and predictable seasonal cycles of phytoplankton growth, while another 21% displays strong year-to-year variations. We also found that subsurface phytoplankton layers, often invisible to satellites, are widespread and represent a significant portion of the total biomass. These findings provide a new view of how biological variability is structured across the Southern Ocean and how it may respond to future climate change.

1. Introduction

The Southern Ocean (south of 30°S) is a critical component of the global oceanic carbon sink, accounting for approximately half of the ~27% of anthropogenic carbon dioxide (CO_2) emissions absorbed annually by the global ocean (Friedlingstein et al., 2025; Mayot et al., 2023). Phytoplankton plays a central role in regulating the Southern Ocean CO_2 sink by assimilating dissolved inorganic carbon, which leads to a maximum air-to-sea CO_2 flux (ocean uptake) during summer in this region (Gruber et al., 2019). However, estimates of the summer air-to-sea CO_2 flux in the Southern Ocean vary widely among global ocean biogeochemical models, reflecting uncertainties in the representation of the magnitude and timing of phytoplankton production and of the associated winter vertical mixing (Gruber et al., 2019; Hauck et al., 2023). In particular, Hauck et al. (2023) show that

summer air-to-sea CO_2 flux uncertainty is largest in ice-free regions, both in terms of inter-model spread and model-observation differences, and that these regions account for most of the basin-integrated net air-to-sea CO_2 uptake (approximately 85%–87%). This highlights the need for refined observational constraints on the spatio-temporal variability of phytoplankton biomass and production to better inform models (Kuhn et al., 2025), and improve simulations and understanding of the Southern Ocean CO_2 sink. Furthermore, since phytoplankton production in the Southern Ocean is projected to change under future climate scenarios (Tagliabue et al., 2021), improving our understanding of biomass variability is essential for accurately projecting future air-to-sea CO_2 fluxes.

Various bioregionalizations of the Southern Ocean have been developed to synthesize and investigate phytoplankton seasonal dynamics and, more broadly, to investigate the biogeochemical functioning of this ocean basin. By synthesizing complex dynamics, these bioregionalizations have helped identify key drivers of Southern Ocean phytoplankton blooms and the Southern Ocean CO_2 sink (e.g., Ardyna et al., 2017; Gregor et al., 2018) and have supported regional evaluations of global ocean biogeochemical models (Hauck et al., 2023). Most of these bioregionalizations rely on surface chlorophyll-*a* concentration (Chl*a*) derived from satellite ocean color imagery to characterize surface phytoplankton biomass variability. Early bioregionalizations of the global ocean suggested a zonal structure within the Southern Ocean aligned with the major fronts of the Antarctic Circumpolar Current (ACC, e.g., Fay & McKinley, 2014; Longhurst, 2007b; Reygondeau et al., 2013). However, more recent approaches, focusing on the Southern Ocean and the seasonal distribution of surface phytoplankton biomass, have revealed significant deviations from this zonal pattern (Ardyna et al., 2017; Thomalla et al., 2011). These departures from the zonal pattern have been primarily attributed to spatial variability in nutrient supply, particularly iron (Ardyna et al., 2017; Graham et al., 2015; Sullivan et al., 1993; Thomalla et al., 2011). In terms of seasonal dynamics, wintertime vertical mixing is recognized as a key driver of phytoplankton biomass, influencing both the entrainment of nutrients and the light environment experienced by phytoplankton, as well as modulating prey-grazer interactions (Behrenfeld, 2010; Llort et al., 2015; Sallée et al., 2015; Tagliabue et al., 2014). Superimposed to the seasonal forcings, sub-seasonal variability, also captured through satellite observations, has been shown to markedly influence seasonal phytoplankton biomass cycles (Fauchereau et al., 2011; Prend et al., 2022; Thomalla et al., 2011). Yet, accounting for the vertical structure of phytoplankton biomass throughout the water column could challenge some of the identified surface-based seasonal and sub-seasonal dynamics (Prend et al., 2022; Sallée et al., 2015).

The magnitude and spatio-temporal variability of vertical phytoplankton biomass in the Southern Ocean remain poorly characterized. It has been shown that depth-integrated phytoplankton biomass can exhibit temporal dynamics that are not captured by surface-derived estimates (Stoer & Fennel, 2024), particularly in the Subantarctic Zone, north of the Subantarctic Front (Sallée et al., 2015; Uchida et al., 2019). This standing stock of phytoplankton biomass, largely undetected by satellites, needs to be better quantified (Stoer & Fennel, 2024). Estimates based solely on the assumption of a uniformly mixed phytoplankton biomass within the surface mixed layer (e.g., Sallée et al., 2015) may underestimate the true stock by ∼50% (Stoer & Fennel, 2024). Moreover, pronounced vertical gradients in phytoplankton biomass have been observed both within the surface mixed layer and immediately below it (Boyd et al., 2024; Carranza et al., 2018), highlighting the importance of accounting for subsurface features.

Deep Chlorophyll Maxima (DCM) can develop under stratified conditions and may structure bioregional patterns of phytoplankton dynamics that remain hidden from satellite surface observations. The mechanisms responsible for their occurrence vary across productivity gradients and regions (Cullen, 2015), as in the Southern Ocean (Baldry et al., 2020). In oligotrophic, subtropical environments of the Southern Ocean (∼30°S–40°S), DCMs often correspond to deep acclimation maxima (DAM), where phytoplankton cells increase their chlorophyll-*a* content relative to carbon biomass under low-light conditions, a photophysiological process known as photoacclimation (Fennel & Boss, 2003). In contrast, in certain conditions, DCMs can represent deep biomass maxima (DBM, Barbieux et al., 2019; Cornec et al., 2021; Hermilly et al., 2025), maintained by growth or aggregations of phytoplankton biomass at depth (Cullen, 2015), and may contribute substantially to water-column production (Barbieux et al., 2022). In the Australian sector around the Polar Front, DCMs associated with DBM have been observed and are suggested to extend across the broader inter-polar frontal zone (Baldry et al., 2020; Boyd et al., 2024). It is therefore essential for an accurate bioregionalization of the Southern Ocean based on the

phytoplankton phenology to take into account potential occurrences of DCMs. Such bioregionalization would then help quantify the spatio-temporal variability of DCM occurrences, determine whether they reflect DBM or DAM, and identify the environmental drivers that induce them.

As these subsurface features are unseen by satellite observations, they must be examined using in situ measurements, such as those provided by Biogeochemical-Argo (BGC-Argo) profiling floats (Sarmiento et al., 2023). In the Southern Ocean, the OneArgo program provides unprecedented in situ biogeochemical observations from BGC-Argo floats, yet its non-gridded, irregular sampling and short record (mostly since 2014) contrast with gridded, long-term (since 1997) satellite data sets (Baudena et al., 2025). BGC-Argo observations can therefore be further enhanced by combining their vertically resolved information on phytoplankton biomass with satellite observations (Sauzède et al., 2016). This approach enables studies of the vertical distribution of phytoplankton biomass over the last two decades at weekly temporal resolution and across an ocean basin (Sauzède et al., 2016), which would not be achievable with either satellite or BGC-Argo data sets alone. Consequently, such a four-dimensional database (latitude, longitude, depth, and time) provides a robust foundation for refining the bioregionalization of the Southern Ocean. Together, the data sets and the resulting bioregionalization will help improve our understanding of phytoplankton biomass dynamics across timescales, from seasonal cycles to interannual and decadal variability.

In fact, beyond seasonal dynamics, the interannual to multiannual variability and long-term trends in phytoplankton biomass in the Southern Ocean continue to be debated (Del Castillo et al., 2019; Liniger et al., 2025). If changes in the position or structure of frontal systems are occurring, which remain to be demonstrated (Chapman et al., 2020), these may be detectable through modifications in phytoplankton biomass-based bioregionalization of the Southern Ocean (Thomalla et al., 2023). To assess this, it is first necessary to establish a robust climatological bioregionalization, and then evaluate temporal variations over recent decades, including the spatial extent affected or remaining stable in the face of such temporal changes.

Emerging changes in environmental conditions, including vertical mixing and sea surface temperature, may already be altering phytoplankton concentrations (Golder & Antoine, 2025; Sallée et al., 2010), with important implications for the Southern Ocean's phytoplankton biogeography (Thomalla et al., 2023). Among large-scale climate drivers, variability associated with the Southern Annular Mode (SAM) exerts one of the strongest influences on the region. Positive SAM phases are linked to a strengthening and poleward shift of the westerly winds. This atmospheric reorganization modifies the Southern Ocean's circulation patterns, as well as the Mixed Layer Depth (MLD), sea surface temperatures, or the sea-ice extent (Sallée et al., 2010; Thompson & Wallace, 2000). Such physical perturbations have cascading effects on biogeochemical processes, including nutrient supply and phytoplankton growth, although their impacts vary across latitudes and sectors of the Southern Ocean (Lovenduski & Gruber, 2005). In this context, a bioregionalization of the Southern Ocean based on phytoplankton phenology provides a powerful framework to disentangle the influence of large-scale climate variability on phytoplankton. This is essential for assessing both ongoing and future changes in the Southern Ocean (Hauck et al., 2015; Mongwe et al., 2024).

In this study, we analyze a 25-year (1998–2022) database of spatially gridded, weekly averaged vertical profiles of Chl*a* and particulate backscattering coefficient (b_{bp}), used as a proxy for phytoplankton carbon. Our goal is to characterize the vertical variability of phytoplankton biomass and how it changes across space and time in the Southern Ocean. First, we establish a bioregionalization of the Southern Ocean based on the seasonal variability of vertical phytoplankton biomass distribution. Unlike previous Southern Ocean bioregionalizations primarily derived from surface satellite Chl*a* products (e.g., Ardyna et al., 2017; Thomalla et al., 2011), our approach is based on an observation-based four-dimensional phytoplankton biomass product that integrates satellite and in situ information. This approach explicitly accounts for the vertical structure of phytoplankton biomass using two complementary proxies, Chl*a* and b_{bp}. Second, we exploit the available 25-year time series of this product to quantify the interannual variability of the resulting bioregionalization, an aspect that has received less attention in previous Southern Ocean bioregionalization studies. Finally, we use this bioregionalization as a spatial framework to advance our understanding of the occurrence and mechanisms driving DCMs in the Southern Ocean, and to assess the influence of the SAM on the interannual variability of phytoplankton biomass.

2. Data and Methods

2.1. Phytoplankton Biomass Data Sets

The vertical distribution of the phytoplankton biomass in the water column can be estimated via two complementary variables: Chl*a* and b_{bp} (Bittig et al., 2019; Boss & Behrenfeld, 2010; Mignot et al., 2014; Stoer & Fennel, 2024; Vives et al., 2024). Although both variables are, to the first order, positively correlated with phytoplankton biomass, they are also influenced by other factors. Chl*a* can also vary in response to changes in the physiological status of phytoplankton cells, for example, photoacclimation (Cullen, 2015; Fennel & Boss, 2003), while b_{bp} variations may also be affected by changes in the nature and size of particles, including non-phytoplankton particles, present in the water column (Bellacicco et al., 2019; Graff et al., 2015; Loisel et al., 2002; Stramski & Kiefer, 1991). Here, we define an observation as the paired vertical profiles of Chl*a* and b_{bp}, which together provide a more consistent proxy for phytoplankton biomass than either variable alone.

Weekly four-dimensional fields (latitude, longitude, depth, and time) of Chl*a* and b_{bp} for the Southern Ocean were extracted from an observation-based global ocean data set (https://doi.org/10.48670/moi-00046) (Sauzède et al., 2016, 2024). This publicly available gridded product spans 25 years (1998–2022), with a horizontal resolution of 0.25° × 0.25°, 36 vertical depth levels: 5-m intervals from 0 to 70 m, 10-m intervals to 100 m, 25-m intervals to 300 m, 50-m intervals to 600 m, and 100-m intervals to 1,000 m.

This gridded product was generated using a neural network developed to infer the vertical distribution of Chl*a* and b_{bp} from satellite observations colocated with in situ vertical profiles of temperature and salinity (Sauzède et al., 2016). This neural network was trained and validated against reference in situ profiles of Chl*a* (Schmechtig et al., 2025) and b_{bp} (Argo, 2025) obtained from BGC-Argo floats. Note that the availability of BGC-Argo profiles was relatively important in the Southern Ocean (Figure S1 in Supporting Information S1), which provides confidence in the Chl*a* and b_{bp} fields derived from this machine learning methodology. To generate a continuous 25-year gridded product, the neural network was applied to 3D fields of temperature and salinity profiles (ARMOR3D product, https://doi.org/10.48670/moi-00052) (Guinehut et al., 2012; Mulet et al., 2012; Verbrugge et al., 2024) merged with remote sensing observations from 1998 to 2022. The observed temperature and salinity profiles from the ARMOR3D data product include profiles from Argo floats, XBT, ship-based CTD casts, and moorings. Those profiles were optimally interpolated by satellite information such as sea surface temperature, sea surface salinity, and sea level anomaly to obtain the ARMOR3D gap-filled product (Guinehut et al., 2012; Mulet et al., 2012).

The gridded product undergoes extensive validation exercises reported in the Quality Information Document (QUID) distributed by the Copernicus Marine Service (https://doi.org/10.48670/moi-00046). The assessment includes (a) validation against a randomly chosen 20% independent subset of the initial BGC-Argo database excluded from model training, (b) validation against independent BGC-Argo float time series excluded from model training, and (c) validation of Chl*a* against an independent global HPLC pigment database. Overall, these validation exercises indicate that the estimated Chl*a* and b_{bp} fields are not affected by systematic biases. The product demonstrates consistently high skill when compared to independent in situ BGC-Argo observations, both globally (Chl*a*: $r^2 = 0.87$, MAPD = 29%; b_{bp}: $r^2 = 0.90$, MAPD = 11%) and in the Southern Ocean (Chl*a*: $r^2 = 0.88$, MAPD = 29%; b_{bp}: $r^2 = 0.93$, MAPD = 17%). As reported in the QUID, the product captures the dominant spatio-seasonal variability of Chl*a* and b_{bp} profiles.

2.2. Clustering Methodology for a Bioregionalization of the Southern Ocean

The objective of our method is to establish a bioregionalization of the Southern Ocean based on the vertical variability of phytoplankton biomass throughout the productive season. To this end, we clustered grid cells of the data product according to the joint vertical structure of Chl*a* and b_{bp} profiles and how this structure evolves over the season. Seasonal variations in vertical phytoplankton biomass structures were first synthesized through two successive principal component analyses (PCAs), and the resulting descriptors were then used in a Gaussian Mixture Model (GMM) clustering. This approach follows previous methodologies that combine dimensionality reduction with unsupervised clustering (Fonvieille et al., 2023; Hardman-Mountford et al., 2008; Jones et al., 2019; Thomas et al., 2021). A graphical overview of the methodology is provided in Figure S2 in Supporting Information S1.

First, weekly climatologies of b_{bp} and Chl*a* profiles were built for each grid cell of the Southern Ocean by averaging data from every year for each week. To capture a consistent signal of Chl*a* and b_{bp} during the productive period, the clustering method considers only grid cells with continuous coverage over the productive season. It was therefore applied to the period from mid-September (38th week) to mid-March (11th week), due to the spatiotemporal limitations of satellite observations from which the Chl*a* and b_{bp} products are derived: Required satellite observations were unavailable during polar night, in sea-ice-covered regions, and under persistent cloud cover. Additionally, Chl*a* and b_{bp} estimates were excluded in areas with bathymetry shallower than 1,000 m. As most of the variations in Chl*a* and b_{bp} occur in the upper water column where phytoplankton production takes place, data from 0 to 100 m at 5-m intervals were selected, with interpolation only at 75, 85, and 95 m. This choice is supported by the fact that in the Southern Ocean, most of the seasonal variance occurs within the upper 100 m (Chl*a*: 93% [86%–97%]; b_{bp}: 90% [83%–94%]; values reported as median [IQR] of the total variance over 0–1,000 m), and it restricts the clustering analysis of the depth range with the highest vertical resolution, avoiding the more extensive interpolation required below 100 m, where the vertical resolution of the product becomes substantially coarser.

Second, two successive principal component analysis (PCAs) were performed to summarize, at each grid cell, the seasonal variability of the paired Chl*a* and b_{bp} profiles. For the first PCA, the input matrix was constructed with rows representing individual grid cell–week combinations (i.e., samples; number of grid cells × 26 weeks), and columns corresponding to the paired vertical profiles of Chl*a* and b_{bp} over 0–100 m. The profiles are normalized by subtracting the ensemble mean and dividing by the ensemble standard deviation. The first PCA produced PCs that summarize the vertical structure of the Chl*a* and b_{bp} profiles. These PCs were then used as inputs for a second PCA designed to capture the dominant modes of their temporal variability. To this end, weekly PC values were concatenated for each grid cell to represent the seasonal cycle. For the second PCA, each sample corresponds to a grid cell, and each variable represents a weekly value from the seasonal time series of the selected PCs from the first PCA. The second PCA was performed on centered data without standardization, which is appropriate given the comparable scales of the variables.

Third, the selected PCs from the second PCA were used as input variables for the clustering analysis, which was performed using a GMM. The GMM requires the number of clusters to be specified a priori and, in return, assigns each grid cell to a cluster based on the similarity of their PC scores. The resulting spatial distribution of clusters defines the bioregionalization. In addition, the GMM provides a membership probability (ranging from 0 to 1) for each grid cell, quantifying the strength of its association with the assigned cluster.

Finally, annual (year-by-year) bioregionalizations for the last 20 years (2002–2022) were generated by extracting annual Chl*a* and b_{bp} data and projecting them onto the clustering framework derived from the climatological analysis described above. Years prior to 2002 (1998–2001) were excluded from this interannual analysis because 15% of the Southern Ocean clustered area in the climatological analysis was missing, compared to only about 6% after 2002. Annual data were defined from mid-September (38th week) of year Y to mid-March (11th week) of year $Y + 1$; for clarity, the corresponding bioregionalization is hereafter referred to as that of year Y. Construction of the annual bioregionalizations involved (a) transforming the annual data from each year using the principal components (PCs) from the first and second PCAs and (b) assigning the resulting projections to clusters using the GMM trained on the climatological data set. Because data coverage was more limited at the annual scale, primarily due to cloud cover and reduced satellite revisit frequency, linear interpolation was applied to fill temporal gaps in Chl*a* and b_{bp} data shorter than 4 weeks.

2.3. Derived Phytoplankton Biomass Features

Following a methodology similar to Cornec et al. (2021), Chl*a* profiles were analyzed to identify the presence of a DCM. Subsequently, b_{bp} profiles were used to determine whether the DCM corresponded to a DBM or a DAM. A DCM was considered present at a given grid cell and time step if the Chl*a* vertical profile exhibited a maximum below 15 m depth, and if this maximum exceeded the median surface (0–15 m) Chl*a* value by at least 40%. A DCM was then classified as a DBM type if the b_{bp} maximum occurred within ±20 m of the DCM depth and was more than 20% higher than the median surface b_{bp} value. Otherwise, the DCM was classified as a DAM type.

In addition to detecting vertical structures, the seasonal dynamics of phytoplankton biomass were also characterized through bloom timing metrics. Specifically, at each grid cell, the timing of the annual bloom was determined. Two bloom-related dates were derived: the bloom climax and the bloom apex (Llort et al., 2015). The

bloom climax corresponds to the date when the rate of net phytoplankton biomass accumulation (r) reaches its maximum, while the bloom apex is the date when r turns negative. These metrics were estimated using a carbon-based proxy of phytoplankton biomass (C_{phyto}; see below), with r defined as

$$r = \left(\frac{1}{P_{int}}\right)\left(\frac{dP_{int}}{dt}\right) \quad (1)$$

where P_{int} is the depth-integrated (0–1,000 m) value of C_{phyto} ($\int C_{phyto}$, in gC m^{-2}) and $dt = 7$ days. Note that the bloom onset (i.e., when r first becomes positive) could not be evaluated due to the scarcity of observations in winter at high latitudes, when bloom initiation likely occurs (e.g., Vives et al., 2024).

The carbon-based estimate of phytoplankton biomass (C_{phyto}) was derived from b_{bp} measurements. Specifically, b_{bp} measured at 700 nm was converted to its equivalent at 470 nm (i.e., b_{bp} (470)) using the relationship: $b_{bp}(470) = b_{bp}(700) \times (470/700)^{-0.78}$ (Boss et al., 2013). Then, b_{bp} (470) was converted into C_{phyto} using the empirical relationship: $C_{phyto} = b_{bp} \times 12{,}128 + 0.59$ (in mgC m^{-3}) (Graff et al., 2015), as previously applied in several Southern Ocean studies based on BGC-Argo data (Lacour et al., 2023; Uchida et al., 2019; Vives et al., 2024).

To limit the inclusion of non-phytoplanktonic particles in the b_{bp}-derived C_{phyto}, we applied a filtering step based on the assumption that phytoplanktonic particles should exhibit a detectable Chl*a* signal. At each grid cell, a specific Chl*a* threshold was defined as the seasonal minimum Chl*a* measured at the depth of the strongest vertical Chl*a* gradient, which typically marks the base of the productive layer (Lacour et al., 2019). The C_{phyto} values at depth were then masked when the corresponding Chl*a* fell below this threshold.

The depth-integrated value of C_{phyto} ($\int C_{phyto}$) is compared with an estimate based on the surface value, similar to the proxy used by Sallée et al. (2015). It corresponds to the surface-averaged (0–10 m) value of C_{phyto} (C^{surf}_{phyto}, gC m^{-3}) multiplied by the depth of the MLD: $C^{surf}_{phyto} \times$ MLD (in gC m^{-2}).

2.4. Environmental Data Sets

The following observation-based data sets, not included in the clustering methodology, are used to support the interpretation of the obtained bioregionalization of the Southern Ocean.

Weekly MLD estimates, between 1998 and 2022 with a 0.25° × 0.25° spatial resolution, come from the observation-based data product ARMOR3D (Guinehut et al., 2012; Mulet et al., 2012). Within this product, weekly global 3D fields of temperature and salinity are first estimated by in situ observations, from which 2D (spatiotemporal) fields of MLD are derived from a dual-criterion approach: the minimum depth where either the temperature has decreased by 0.2°C from the surface or the density reaches the value expected for surface water cooled by 0.2°C. Stratification was quantified using the Brunt-Väisälä frequency (N^2), computed from ARMOR3D profiles of temperature and salinity via the TEOS-10 equation of state.

Monthly climatological profiles of nitrate concentrations, between 0 and 800 m and at a 1° × 1° spatial resolution, are obtained from the World Ocean Database 2023 (Garcia et al., 2024). This data set corresponds to the objectively analyzed climatological mean fields obtained by with all available in situ measurements between 1965 and 2022.

The observation-based estimate of the winter SAM index was downloaded from http://www.nerc-bas.ac.uk/icd/gjma/sam.html (Marshall, 2003). This index is derived from mean sea level pressure measurements at land-based stations. This estimated SAM index is based on an empirical definition that calculates the zonal mean sea level pressure difference between 40°S and 65°S (Gong & Wang, 1999).

3. Results

The Results section is organized as follows. Section 3.1 provides an overview of the general spatial distribution of the clusters from a latitudinal perspective and their associated annual cycles of phytoplankton biomass, thereby defining the climatological (mean) bioregionalization of the Southern Ocean. Section 3.2 examines the inter-annual variability of this bioregionalization by distinguishing core (temporally persistent) and non-core areas, and by evaluating, for each year, the consistency of grid-cell assignments (i.e., membership probabilities) within these

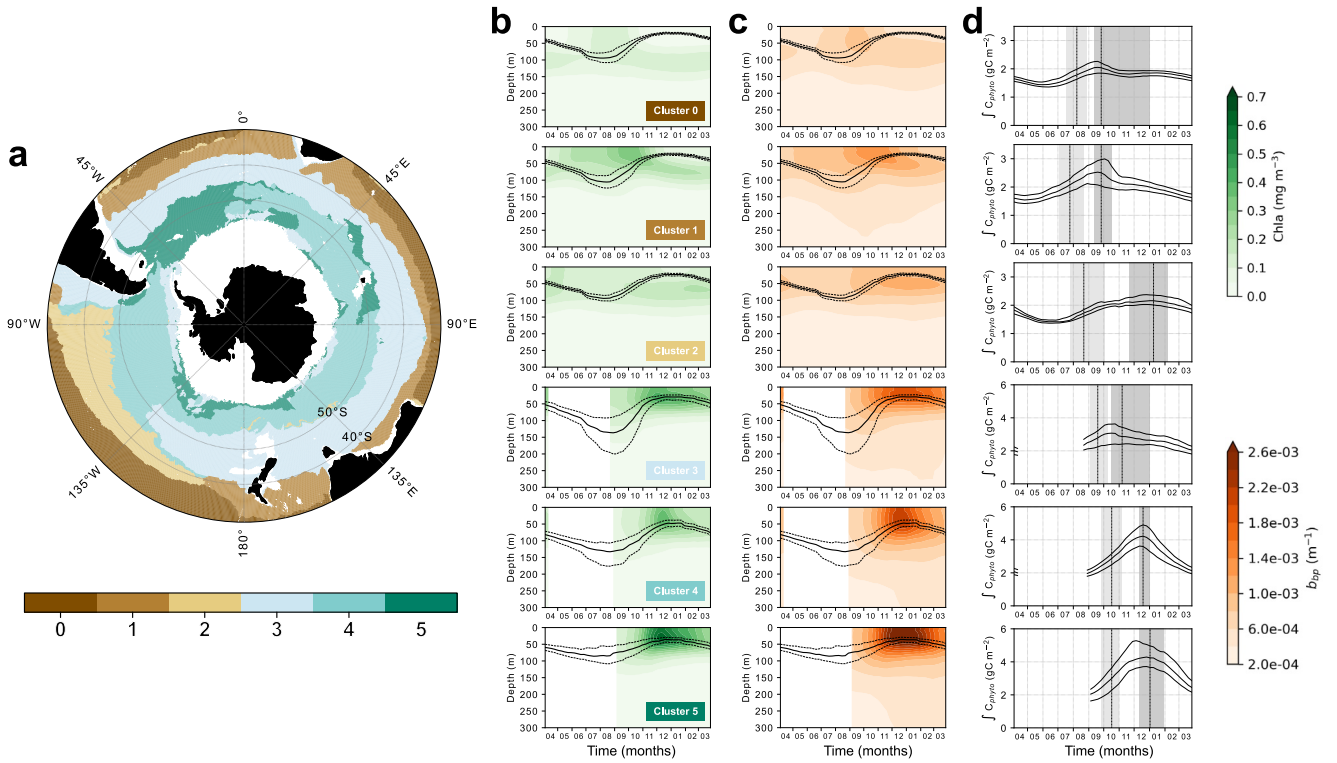

Figure 1. Bioregionalization of the Southern Ocean based on phytoplankton phenology. (a) Spatial distribution of the obtained clusters (i.e., bioregions). White areas indicate locations with no data available (see Section 2.2). (b, c) Annual time series of vertical profiles of Chl*a* (green) and b_{bp} (orange). Black lines indicate the median mixed layer depth, with dashed lines showing the interquartile range. (d) Depth-integrated (0–1,000 m) median time series of C_{phyto}, with interquartile range. Light and dark gray areas indicate the interquartile ranges of bloom climax and bloom apex timing, respectively; dashed lines indicate their median dates. In panels (b–d), white areas denote weeks where data are missing in 10% or more of the grid cells associated with each cluster.

areas. Based on these probabilities, the analysis estimates the mean annual fraction of the Southern Ocean exhibiting expected phytoplankton phenology, interannual variability, or undefined phenology. Section 3.3 investigates the occurrence of subsurface phytoplankton biomass maxima in the Southern Ocean, taking advantage of the temporally continuous gridded data set of paired Chl*a* and b_{bp} profiles and the spatial framework provided by the bioregionalization. Finally, Section 3.4 analyzes the influence of interannual variations in MLD, modulated by the SAM, on phytoplankton biomass, again leveraging the coherent gridded data sets of MLD and phytoplankton biomass within the established biogeographic framework.

3.1. The Bioregionalization of the Southern Ocean

The Southern Ocean was partitioned into six coherent bioregions (Figure 1a), each defined by distinct seasonal variations in vertical phytoplankton biomass (Figures 1b–1d). To achieve this, two successive PCAs were applied, yielding a reduced set of components that captured both the diversity and the dominant modes of seasonal variability in vertical phytoplankton biomass (Text S1; Figures S3–S4 in Supporting Information S1). The three PCs retained from the second PCA explained 88% of the variance and displayed distinct spatial patterns (Figure S4 in Supporting Information S1). These components were then used as input to a GMM clustering, which identified six spatially coherent clusters interpretable as bioregions (Figure 1a), despite geolocation not being an input variable. The GMM required the number of clusters, k, to be specified a priori. Several values of k were tested, and $k = 6$ was found to best capture the diversity of features while maintaining a reasonable number of biologically interpretable clusters. This choice, although partly subjective, was supported by the Bayesian Information Criterion, which shows a strong decrease up to $k = 6$ and only limited improvement beyond (Figure S5 in Supporting Information S1). This choice was further supported by the fact that each of the six bioregions exhibited distinct seasonal variations in Chl*a* and b_{bp} in the upper water column (Figures 1b and 1c). Furthermore, grid-cell membership probabilities were high (median 0.95–0.99) and well above those of the second most probable cluster, confirming that most grid cells were unambiguously associated with a single cluster and

supporting the robustness and spatial coherence of the identified bioregions. Sensitivity tests indicate that $k = 5$ tends to merge the northernmost regions and weaken key boundaries, whereas the additional splitting at $k = 7$ is associated with increased local classification uncertainty, supporting the choice of $k = 6$.

Clusters 0 and 1 are located in the northernmost regions of the Southern Ocean (north of ~40°S) and represent 23% of the Southern Ocean clustered area (Figure 1a). In these clusters, the depth-integrated (0–1,000 m) phytoplankton biomass (i.e., $\int C_{phyto}$) strongly increases in austral winter (June, July, and August) and peaks in spring (September $\int C_{phyto}$ in Cluster 0 = 2.06 gC m^{-2} and in Cluster 1 = 2.53 gC m^{-2}, Figure 1d). Then, the phytoplankton biomass develops around a DCM in summer (December, January, and February; Figures 1b and 1c) located ~117 m in Cluster 0 and ~73 m in Cluster 1. When using a proxy for the water-column phytoplankton biomass $\left(C_{phyto}^{surf} \times MLD\right)$, the $\int C_{phyto}$ in these two clusters is underestimated, mostly in summer due to the presence of subsurface phytoplankton biomass (Figure S6 in Supporting Information S1). On average, over the seasonal cycle it results in a ~11.6 TgC underestimation by the $\left(C_{phyto}^{surf} \times MLD\right)$ proxy into these two clusters. The north-south distinction between the two clusters is partly related to higher winter and spring Chl*a* and b_{bp} values in Cluster 1 (southern) than in Cluster 0 (northern) (Figures 1b and 1c). Cluster 0 is characterized by the lowest depth-integrated phytoplankton biomass values throughout the spring-summer seasons among all Southern Ocean regions ($\int C_{phyto}$ = 1.88 gC m^{-2}).

In contrast, Clusters 4 and 5 are located in the southernmost part of the Southern Ocean (south of ~50°S) (Figure 1a). They represent 37% of the Southern Ocean clustered area. In these clusters, the depth-integrated phytoplankton biomass increases in spring (September, October, November), and reaches its maximum ($\int C_{phyto}$ ~ 4.25 gC m^{-2}) in early summer (December), later than in all the other clusters located at lower latitudes (Figure 1d). Cluster 5 is associated with regions downstream of islands and shallow topographic features that disrupt the ACC, whereas Cluster 4 is associated with the open-ocean realm (Figure 1a). The annual phytoplankton biomass is higher in Clusters 4 and 5 than in any of the other clusters. It lasts longer in Cluster 5 (~2 months) than in Cluster 4 (1 month), leading to a higher depth-integrated phytoplankton biomass in Cluster 5 (the island/topography-influenced region) than in Cluster 4 (spring-summer averaged $\int C_{phyto}$ in Cluster 4 = 3.21 gC m^{-2} and in Cluster 5 = 3.53 gC m^{-2}). The estimated $\int C_{phyto}$ by the $\left(C_{phyto}^{surf} \times MLD\right)$ proxy in these two clusters are primarily underestimated in summer (~60% of missed biomass, Figure S6 in Supporting Information S1). Because the spatial extension of Cluster 5 is smaller than Cluster 4, it results in an underestimation of $\int C_{phyto}$ by the $\left(C_{phyto}^{surf} \times MLD\right)$ proxy on average over the seasonal cycle of ~11 TgC in Cluster 5 and ~22.1 TgC in Cluster 4.

Clusters 2 and 3 are located at mid-latitudes of the Southern Ocean (~40°S–50°S), between the northernmost (Clusters 0 and 1) and southernmost (Clusters 4 and 5) regions (Figure 1a), and represent 40% of the Southern Ocean clustered area. Cluster 2 is confined to the eastern Pacific Ocean, while Cluster 3 extends across all three basins and lies slightly farther south than Cluster 2 (Figure 1a). In Cluster 2, phytoplankton biomass develops around a DCM during summer (~71 m), similar to patterns observed at lower latitudes, but without a preceding spring maximum (Figures 1b and 1c). Therefore, Cluster 2 presents an underestimation of $\int C_{phyto}$ by the $\left(C_{phyto}^{surf} \times MLD\right)$ proxy similar to the northernmost clusters (~8 TgC, Figure S6 in Supporting Information S1). In contrast, Cluster 3 does not display a summer DCM but has a spring depth-integrated phytoplankton biomass maximum ($\int C_{phyto}$ = 3.08 gC m^{-2}) higher than in the northernmost Clusters 0 and 1 ($\int C_{phyto}$ ~ 2.3 gC m^{-2}, Figure 1d). However, its annual biomass peak is lower in magnitude and occurs earlier in the year than in the southernmost Clusters 4 and 5 ($\int C_{phyto}$ ~ 4.25 gC m^{-2}, Figure 1d). Nonetheless, Cluster 3 has the largest spatial extension and therefore the largest underestimation of $\int C_{phyto}$ by the $\left(C_{phyto}^{surf} \times MLD\right)$ proxy: ~26.1 TgC (Figure S6 in Supporting Information S1).

3.2. Interannual and Spatial Variability of the Bioregions

Annual bioregionalizations for 2002–2021 were computed to assess the interannual variability of the six climatological clusters previously identified (Section 3.1). The resulting annual bioregionalizations are consistent with the climatological clustering as indicated by similar statistics to the ones obtained with the climatological data sets (Figure S7 in Supporting Information S1). First, the membership probabilities of grid cells annually assigned to each cluster are high (median values between 0.87 and 0.99), although slightly lower than the membership probabilities obtained for the climatological clustering. Second, the spatial variability of the

10.1029/2025GB008930

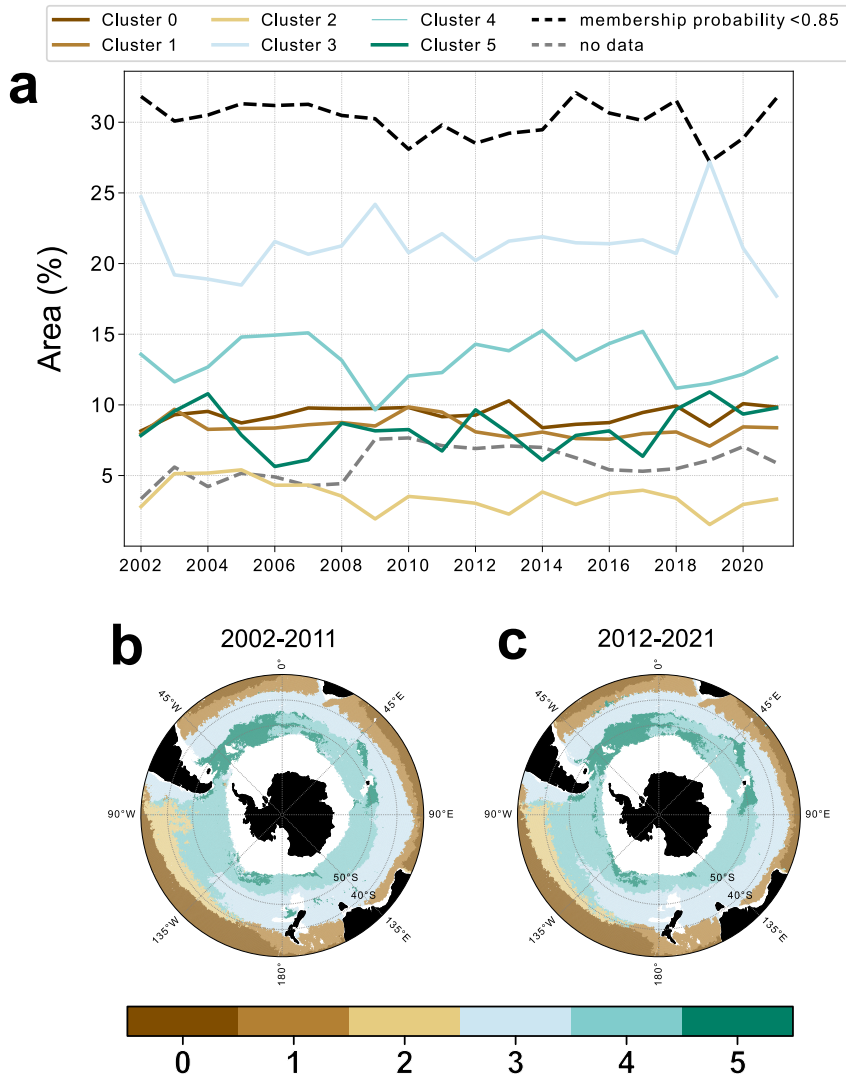

Figure 2. Temporal evolution of the Southern Ocean bioregionalization. (a) Spatial extent of the different clusters over the past 20 years. Only pixels with a membership probability ≥0.85 to a given cluster are considered. The spatial extent of areas with a membership probability <0.85 is shown with a dashed dark line, while that of unclassified areas (no data) is shown with a dashed gray line. (b, c) Decadal averages of annual bioregionalizations for the periods (b) 2002–2011 and (c) 2012–2021, respectively.

membership probabilities to a given cluster was similar between the climatological and annual clustering, with the border areas between clusters displaying lower membership probabilities (<0.85) than the areas located at the center of the clusters (Figures S7c and S7d in Supporting Information S1). Finally, the bioregion map obtained by averaging the 20 annual maps was similar to the bioregion map obtained with the 25-year long climatological data set (Figure S7a and S7b in Supporting Information S1). The consistency between the mean of the annual bioregionalizations and the climatological bioregionalization indicates that the annual data sets and their derived bioregionalizations capture meaningful patterns rather than noise.

The bioregionalization of the Southern Ocean has remained relatively stable over the past 20 years (Figure 2). Between 2002 and 2021, none of the bioregions exhibited a strong temporal trend of either spatial expansion or contraction (Figure 2a). These trends were evaluated using only grid cells with high membership probabilities (≥0.85), ensuring that the analysis focused on the most robust assignments. The average maps for the last (2012–2021) and preceding (2002–2011) decades were broadly similar (Figures 2b and 2c), with a minor exception for Cluster 5, which appeared more frequently south of Tasmania during the first decade, and was more prominently observed in the Pacific sector during the second decade.

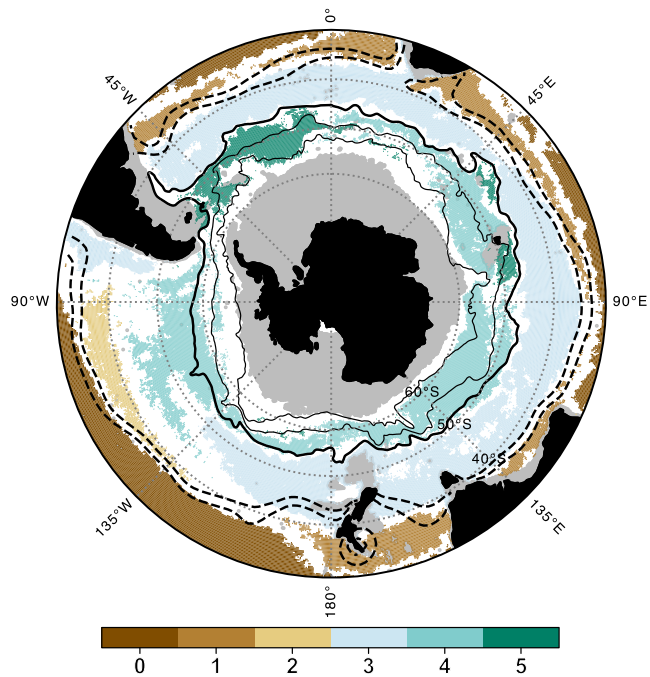

Figure 3. Core areas of the Southern Ocean bioregionalization. Gray areas indicate locations with no data available. Colored areas represent core areas where a given cluster appears in at least 75% of the 20 annual bioregionalizations; otherwise, the area is shown in white. Solid black lines indicate the positions of the three major Antarctic Circumpolar Current (ACC) fronts, from north to south: the Subantarctic Front (in bold), the Polar Front, and the Southern ACC Front. Dashed contour lines indicate surface nitrate concentrations of 1–2 μmol kg^{-1} (annual average).

A cluster stability map (Figure 3) illustrates the temporal persistence of the phenological regimes identified by the clustering, with colors showing the most frequently assigned cluster for each grid cell over the 20 years analyzed. This analysis reveals two distinct categories: core areas, where grid cells remained in the same cluster for at least 75% of the years, and non-core areas (shown in white in Figure 3), where persistence was below 25%. Core areas dominate, covering 58% of the Southern Ocean, and are generally found at the centers of cluster domains, whereas non-core areas (42%) occur mainly along their boundaries.

While the spatial boundaries of core and non-core areas remain stable over time, the membership probabilities within these areas fluctuate annually (Figures 2a and 4). On average, ∼43% of the Southern Ocean within core areas (about three-quarters of core areas) exhibit high membership probabilities in a given year, indicating recognizable climatological patterns of phytoplankton phenology. These regions are categorized as *expected*. In parallel, ∼21% of the Southern Ocean within non-core areas also show high annual membership probabilities, hereafter referred to as the *interannual* category (see next paragraph). Together, this means that in any given year ∼64% of the Southern Ocean can be robustly assigned to recognizable phenology patterns, divided between *expected* (∼43%) and *interannual* (∼21%). The remaining ∼30% exhibit low membership probabilities and are therefore categorized as *undefined*. These proportions (43% *expected*, 21% *interannual*, 30% *undefined*) represent typical annual distributions, although the exact fractions vary from year to year as membership probabilities fluctuate.

Most of the observed interannual variability within the ∼64% of the Southern Ocean characterized by recognizable phenological patterns occurred in non-core areas (the *interannual* category). On average, the amplitude of interannual fluctuations in cluster surface area was 1.61 ± 0.49 times greater in non-core than in core areas (standard deviation of the detrended time series, Figure S8 in Supporting Information S1). Moreover, Figure 2a shows that some time series from adjacent clusters were negatively correlated: the two mid-latitude Clusters (2 and 3) tended to reorganize in opposition to one another (Spearman correlation coefficient, $r_s = -0.66$), as did the high-latitude Clusters (4 and 5, $r_s = -0.63$). Overall, these results suggest that most year-to-year variability in phytoplankton phenology occurs in non-core areas (the *interannual* category in Figure 4), particularly in the mid- and high-latitude bands.

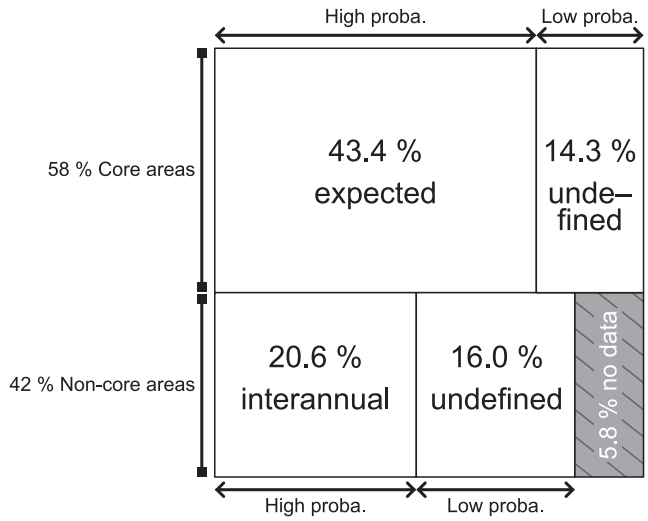

Figure 4. Mean distribution of the Southern Ocean surface area among the categories (see Section 3.2) defined from annual membership probabilities over 2002–2021. On average, 64% of the Southern Ocean is robustly assigned (high membership probability) to a recognizable climatological cluster, including 43% in core areas (*expected* category) and 21% in non-core areas (*interannual* category). Each year, about 30% of the area exhibits low membership probabilities (*undefined* category; 14% in core areas, 16% in non-core areas), while 6% remains unclassified due to missing data.

Approximately 30% of the Southern Ocean exhibits unclear phytoplankton phenology each year (the *undefined* category), as defined by cluster membership probabilities below 0.85 (black dotted line in Figures 2a and 4). Of this fraction, ~16% lies within non-core areas (Figure 4), while the remaining ~14% is unexpectedly located within core regions (Figure 4), primarily south of 40°S. This indicates that substantial and unpredictable temporal variability in phytoplankton phenology can also occur within core areas typically considered stable.

In summary, each year, ~43% of the Southern Ocean within core areas exhibit expected climatological patterns of phytoplankton phenology (*expected* in Figure 4). An additional ~21% of the area, located in non-core regions, is associated with year-to-year variability, mainly between adjacent mid- and high-latitude clusters (*interannual* in Figure 4). The remaining Southern Ocean area shows undefined phenological patterns (~30%, *undefined* in Figure 4) or remains unclassified (~6%, *no data* in Figure 4) due to missing data (gray dotted line in Figures 2a and 4).

3.3. Occurrence of Deep Phytoplankton Biomass Maxima

In low latitude regions (30°S–40°S), a DCM can be present for more than 50% of the year (Figure 5a). These regions are associated with the northernmost Clusters (0 and 1), as well as with the mid-latitude Cluster 2. In some restricted areas of Cluster 0, a DCM can even be present all year long (Figure 5c). Note that the absolute Chl*a* and b_{bp} values associated with this subsurface feature may be slightly underestimated, likely due to the relatively coarse vertical resolution of the gridded product below 100 m (e.g., Figure 6a; see also the product QUID for further details).

In the Pacific sector of Cluster 0, the DCM primarily corresponds to a DAM, with no evidence of a DBM (Figures 5b and 5c). Here, a DAM refers to a Chl*a* maximum not accompanied by a co-located b_{bp} maximum (i.e., no evidence of subsurface biomass accumulation), whereas a DBM-type DCM indicates a Chl*a* maximum co-occurring with a b_{bp} maximum, consistent with a true subsurface biomass accumulation. In contrast, in other low-latitude regions (including the Atlantic and Indian sectors of Cluster 0), the nature of the DCM evolves over the summer season: it initially reflects a DAM but transitions to a DBM about 1 month later (Figure 5c). The time of the DCM formation also differs across clusters, emerging in early September in Cluster 0 and in late October in Clusters 1 and 2 (Figure 5c). The emergence of the DCM occurs just after the seasonal maximum in Chl*a* within the surface mixed layer. Thereafter, surface concentrations of Chl*a* progressively decline while the depth and magnitude of the DCM increase, a pattern most clearly observed in Cluster 1 (Figure 6).

At higher latitudes (>50°S), substantial occurrences of a DCM (10%–30% of the year) are detected south of the Polar Front (Figures 5a and 5b). These DCMs are primarily found within Cluster 4, where their presence peaks in January but remains restricted to less than 40% of the cluster's core area (Figure 5c). Within this high-latitudinal band, DCMs corresponding to a DBM are mostly confined to the region south of Australia (Figures 5a and 5b). The establishment of the DCM typically occurs in November, just below the MLD (Figure 6). Unlike in lower latitude regions, where DCM formation coincides with declining surface biomass, the first two months following DCM establishment in Cluster 4 are marked by continued increases in surface Chl*a* and b_{bp}, both peaking in December. During this period, the magnitude of the DCM also intensifies (Figure 6).

3.4. Relationships Between Phytoplankton Biomass, MLD and SAM Index

The influence of large-scale climate variability, as represented by the SAM index, on environmental drivers of phytoplankton dynamics was assessed across the core areas of the bioregions. The strongest relationships with maximum winter MLD were detected in two latitudinally contrasted clusters: the low-latitude Cluster 1 and the high-latitude Cluster 4. To detect this, we first identified the maximum winter MLD at each grid cell, and for each year between 1998 and 2021. Next, the 24-year time series of maximum winter MLD at each grid cell was detrended by removing long-term trends, and for each year, median values were computed across the core area of

10.1029/2025GB008930

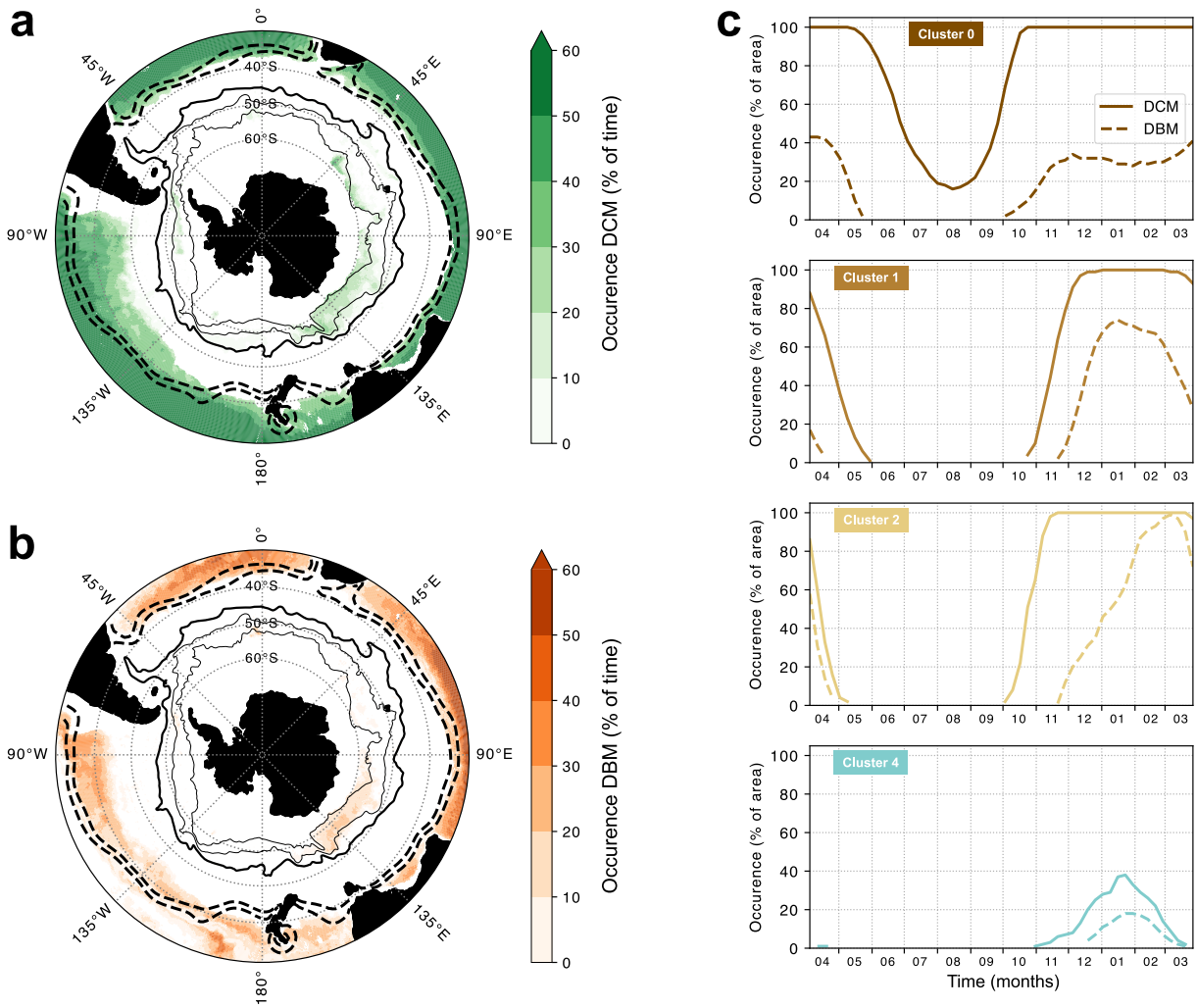

Figure 5. Climatological occurrences of deep chlorophyll maxima (DCM) and deep biomass maxima (DBM) in the Southern Ocean. Maps of the occurrence over an annual cycle of the (a) DCM and (b) DBM features, derived from the 25-year climatological data set of Chl*a* and b_{bp}. Solid black lines indicate the positions of the three major Antarctic Circumpolar Current (ACC) fronts, from north to south: the Subantarctic Front (in bold), the Polar Front, and the Southern ACC Front. Dashed contour lines indicate surface nitrate concentrations of 1–2 µmol kg^{-1} (annual average). (c) Spatial occurrence of DCM and DBM over the annual cycle in the core areas of Clusters 0, 1, 2, and 4.

each cluster. Finally, for each cluster, we assessed the relationship (Spearman correlation coefficient) between the detrended 24-year time series of median maximum winter MLD and the corresponding winter SAM index values. High correlation values ($|r_s| > 0.5$) were found for two clusters: the low-latitude Cluster 1 exhibited a negative correlation ($r_s = -0.56$), while the high-latitude Cluster 4 showed a positive correlation ($r_s = 0.64$).

The influence of winter MLD on the seasonal patterns of phytoplankton biomass was assessed by examining its relationship with biomass levels during the blooming period between 2002 and 2021. For each year, anomalies of $\int C_{phyto}$ were defined as the weekly deviations from the long-term weekly climatology. These anomalies were then averaged between the bloom climax and apex dates, as identified from the climatological cycle (Figure 7). The median of these values was computed across the core area of each cluster. Finally, the relationship between the detrended (removing long-term trends) 20-year time series of median maximum winter MLD and blooming-period phytoplankton biomass was evaluated. Cluster 1 exhibited a moderate positive correlation ($r_s = 0.43$), suggesting that deeper MLD may enhance bloom biomass. In contrast, Cluster 4 showed no significant correlation ($r_s = -0.27$). We also assessed the relationship between the winter SAM index and bloom-period biomass; correlations were generally weaker than for SAM-MLD and MLD-biomass (Cluster 1: $r_s = -0.24$; Cluster 4:

10.1029/2025GB008930

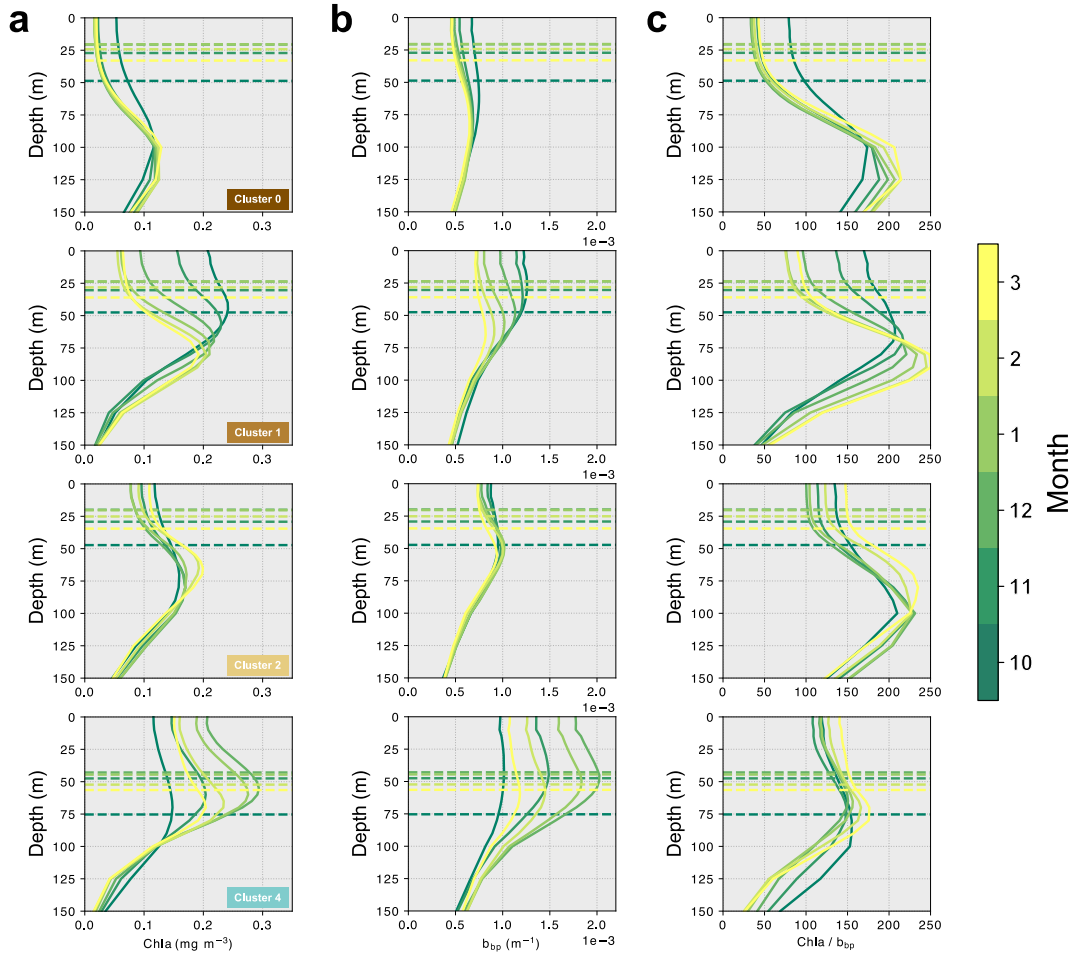

Figure 6. Temporal evolution of Chl*a* and b_{bp} profiles associated with a deep chlorophyll maxima (DCM) in the Southern Ocean. For Clusters 0, 1, 2, and 4, mean monthly vertical profiles of (a) Chl*a* and (b) b_{bp} from October to March. The monthly mixed layer depth is represented by a dotted line. For each cluster's core area, the monthly average was calculated with the Chl*a* and b_{bp} profiles taken from grid cells that displayed a DCM at least once between October and March.

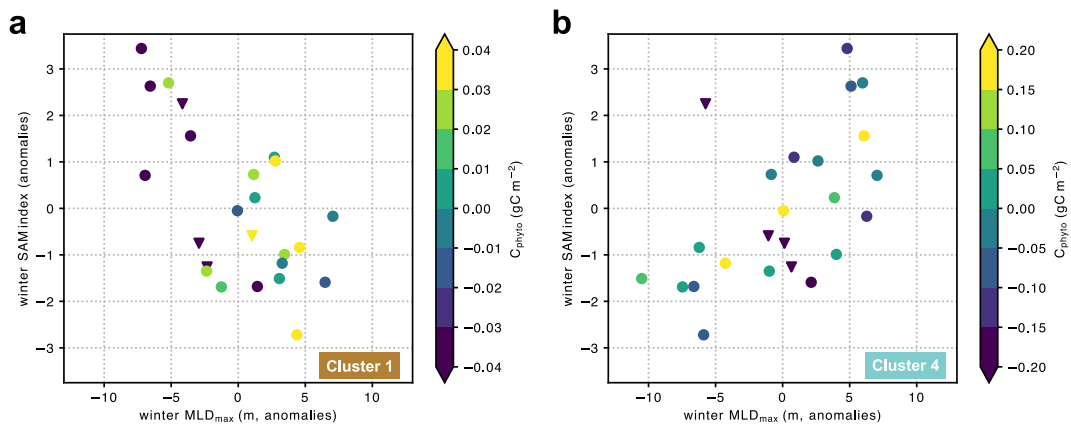

Figure 7. Influence of the Southern Annular Mode (SAM) index on the winter mixed layer depth (MLD) and the blooming phytoplankton biomass in the subtropical and antarctic regimes. Scatter plot showing the relationship between winter SAM index anomalies and anomalies in maximum winter MLD (MLD_{max}) for Clusters 1 (a) and 4 (b). Each dot represents a specific year and is colored according to the anomaly in blooming-period phytoplankton biomass (C_{phyto}). Downward-pointing triangles indicate years (1998–2001) with insufficient data coverage to reliably estimate C_{phyto}.

$r_s = -0.09$). Overall, these results suggest an indirect SAM influence on blooming-period phytoplankton biomass in Cluster 1 mediated by winter mixing, rather than a basin-wide direct SAM control.

4. Discussion

4.1. The Southern Ocean Bioregions and Their Boundaries

Three major regimes emerge from the vertical and seasonal variability of phytoplankton biomass in the Southern Ocean (>30°S). The northernmost, mid-latitude, and southernmost clusters correspond to the subtropical, subantarctic, and antarctic regimes, respectively, as previously identified (Sallée et al., 2015). The largest bioregions correspond to the subantarctic Cluster 3 and the antarctic Cluster 4, which together represent 58% of the classified Southern Ocean area. Our results indicate that estimates of water-column integrated phytoplankton biomass based solely on surface concentrations and mixed-layer depth (e.g., Sallée et al., 2015) likely underestimate biomass stocks in these two regions by ~48.1 ± 32.4 TgC (38.5% ± 15.2%) on average over the seasonal cycle. In addition, our analysis delineates two clear boundaries separating the subtropical, subantarctic, and antarctic regimes, which coincide with known oceanographic features (Figure 3). Finally, the results confirm the presence of non-latitudinal patterns within each regime, as previously suggested from surface satellite observations (Ardyna et al., 2017). Here, we further support this non-latitudinal organization using a vertically resolved data set.

First, the boundary between the subtropical clusters (0 and 1) and the subantarctic clusters (2 and 3) coincides with a southward increase in surface nitrate concentrations as determined from the World Ocean Database (Garcia et al., 2024), which reach average annual values of 1–2 μmol kg^{-1} (Figure 4). These nitrate levels may serve as a spatial threshold distinguishing regions where phytoplankton production is primarily limited by nitrate versus iron (Longhurst, 2007a; Weis et al., 2024). This finding supports the idea that nutrient availability is one of the key drivers of large-scale seasonal variability in vertical phytoplankton distributions (Bock et al., 2022). Note that the term subantarctic regime was preferred over alternatives, such as *Subtropical Seasonally Stratified Biome* (Fay & McKinley, 2014) or *Transition Zone* (Thomalla et al., 2011), to emphasize its distinct biogeochemical identity. Although this region has at times been described as a transitional zone, for example, for southern and subtropical fish populations (Hunt et al., 2016; Rintz et al., 2025), the terminology adopted here reflects the central role of iron limitation in shaping the boundary between the subtropical and subantarctic clusters.

Further south, the boundary between the subantarctic clusters (2 and 3) and antarctic clusters (4 and 5) corresponds to the location of the Subantarctic Front. The position of this front is here derived from satellite altimetry data (Park & Durand, 2019). In previous bioregionalizations of the Southern Ocean, such as the one proposed by Longhurst (2007b), the Polar Front was used as the southern boundary. However, it has been demonstrated that the phytoplankton phenology and biomass are significantly different north and south of the Subantarctic Front (Sallée et al., 2015). This front is also marked by a sharp surface temperature drop, typically below 8°C (Park et al., 2019), which has been used to delineate biomes in other classification schemes (e.g., Fay & McKinley, 2014). Note that in the eastern Pacific sector, the subantarctic Cluster 4 tends to extend further north across the Subantarctic Front, which could be explained by the ephemeral occurrence of fronts in this sector, with enhanced latitudinal variability because it is less constrained by bathymetric features than in the western Pacific sector (Chapman, 2017; Chapman et al., 2020).

The latitudinal gradient in the timing of the phytoplankton bloom is clearly evident in our results (Figures 1b–1d), consistent with previous observations (Ardyna et al., 2017; Simon et al., 2025). The bloom climax (maximum of the phytoplankton biomass accumulation rate, r) occurs in winter (July–August) in subtropical regions, in late winter/early spring (August–September) in subantarctic regions, and in spring (October) in the antarctic regions. This confirms the importance of the light limitation in early spring as one of the main environmental drivers of the phytoplankton production (Boyd, 2002) and of the latitudinal patterns in phytoplankton phenological regimes (Ardyna et al., 2017; Bock et al., 2022; Simon et al., 2025).

Iron availability is widely recognized as a key driver of the non-zonal spatial organization of phytoplankton biomass dynamics in the Southern Ocean (Graham et al., 2015; Sullivan et al., 1993). In the ice-free Southern Ocean considered here, the dominant pathways of iron supply likely vary regionally and include atmospheric deposition (e.g., Cassar et al., 2007; Weis et al., 2024), sedimentary inputs associated with shallow bathymetric features and circulation-topography interactions (e.g., Blain et al., 2007), meltwater-related input (e.g., Lannuzel et al., 2010), and localized sources such as hydrothermal vents (e.g., Ardyna et al., 2019). Differences in the

relative importance of these pathways can sustain contrasting bloom magnitude and duration by alleviating iron limitation over distinct spatial and temporal scales. This heterogeneity is particularly pronounced in our antarctic clusters (4 and 5), where the longer-lasting bloom observed in Cluster 5 compared to Cluster 4 may be associated with stronger or more persistent regional iron inputs. In the Atlantic sector, the broad spatial extent of antarctic Cluster 5 may reflect the convergence of multiple iron supply mechanisms, including dust deposition, shallow bathymetric features, and ice melt (Ardyna et al., 2017; Boyd et al., 2012). In contrast, in the Indian sector, the more spatially confined presence of Cluster 5 likely corresponds to phytoplankton blooms developing over the continental shelves and downstream of the Crozet and Kerguelen islands (Blain et al., 2007; d'Ovidio et al., 2015). We note that sea-ice related iron pathways are only partially represented in our ice-free domain, and extending the framework into the seasonal ice zone would allow a more explicit assessment of under-ice and shelf-controlled iron supply.

4.2. Spatiotemporal Variability of the Identified Bioregions

Our analysis indicates high spatio-temporal variability of the phytoplankton phenology in the Southern Ocean, with 42% of non-core areas identified (Figure 4). This is consistent with the concept of areas with low reproducibility of climatological seasonal cycles of surface phytoplankton biomass introduced by Thomalla et al. (2011, 2023), while extending this framework to vertically resolved biomass variability. The largest area of variability was observed in the eastern Pacific sector between 40°S and 50°S (Thomalla et al., 2011), which aligns with a large non-core area identified in our analysis, located between the subantarctic and antarctic regimes (white area in Figure 3). Another area showing similar characteristics (i.e., non-core area and low reproducibility) is found in the antarctic regime, specifically in the Atlantic and western Indian sectors, and along the ice edge in the Pacific Ocean.

Approximately half of the non-core areas are induced by the interannual variability within the spatial extension of the subantarctic and antarctic clusters (Figure S8 in Supporting Information S1). The eastern Pacific sector encompasses the transition zone between the subantarctic clusters, where their interannual variability reaches its maximum (Figure 3). The dominant mode of multi-annual variations of surface Chl*a* detected in this region by Prend et al. (2022) is consistent with the significant interannual variations observed in our study. In the antarctic region, the interannual variability in the occurrence of Cluster 5 along the ice edge could be induced by the influence of the ice as a natural iron source for phytoplankton production (e.g., Lannuzel et al., 2010). In the last decade, the frequency of occurrence of antarctic Cluster 5 has increased along the ice edge in the Pacific sector (Figure 2c) and matched with the higher surface Chl*a* observed in this region during the recent decade (Thomalla et al., 2023). Such decadal variations could be induced by the particularly important reduction in antarctic sea ice extent since 2016 (Eayrs et al., 2021), which might also influence the phytoplankton communities (Hayward et al., 2025).

Each year, a significant fraction of the Southern Ocean (~30%) appears to have undefined phenological patterns, reflecting locations where phytoplankton dynamics do not align with climatological seasonal cycles identified through our bioregionalization (Figure 4). Such areas with grid cells associated with low membership probabilities to a given cluster, which are different from one year to another, could indicate regions where Chl*a* and b_{bp} variations are more likely driven by sub-seasonal processes. These undefined regions represent a large fraction of the non-core areas (~16% of the Southern Ocean, Figure 4), particularly within the subantarctic and antarctic regimes. This is consistent with earlier findings that sub-seasonal scale variability is more pronounced at higher latitudes of the Southern Ocean (Prend et al., 2022; Thomalla et al., 2011).

4.3. Environmental Controls of Vertical and Interannual Phytoplankton Biomass Variability

4.3.1. Regional Drivers of Subsurface Phytoplankton Biomass

Subsurface maxima in phytoplankton biomass, that is, DBMs, are observed across all three phenological regimes of the Southern Ocean: subtropical, subantarctic, and antarctic. In the subtropical Cluster 0, DBM occurrences are sparser, covering less than 40% of the cluster's core area and confined to the Atlantic and Indian sectors (Figure 5). In contrast, in the subtropical Cluster 1 and the subantarctic Cluster 2, DBMs are more frequent, particularly in January and February. These months are also marked by strong increases in the Chl*a*:b_{bp} ratio with depth (Figure 6), suggesting that photoacclimation processes contribute alongside biomass accumulation to the formation of DCMs in these subtropical and subantarctic regions. The development of DCMs in these regions could be partly driven by increased light availability at depth, as indicated by the concurrent decline in surface Chl*a*

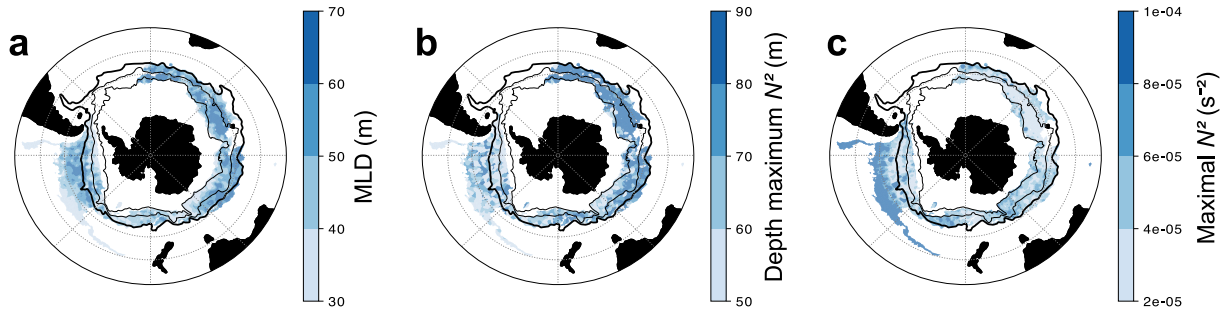

Figure 8. Spatial variability of water-column stratification in Cluster 4 during January. January climatological averages of (a) mixed layer depth, (b) depth of the maximum N^2, and (c) the corresponding maximum N^2 value. The black lines correspond to the climatological locations of the major Antarctic Circumpolar Current fronts (as in Figure 3).

when subsurface maxima emerge (Figure 6; Cornec et al., 2021). In the nitrate-limited subtropical clusters, differences in DCM depth (deeper in Cluster 0 than in Cluster 1) likely reflect variations in nitracline depth (Figure S9 in Supporting Information S1), potentially requiring phytoplankton to grow at different depths.

In the antarctic region, the DBM is located just below the MLD. The Chl*a*:b_{bp} ratio shows a modest increase with depth, peaking near the DBM, indicating some small degree of photoacclimation (Figure 6). Moreover, light availability may play a limited role in shaping subsurface phytoplankton growth in this regime. As observed by Boyd et al. (2024), surface Chl*a* continues to increase even as subsurface maxima in Chl*a* and b_{bp} develop (Figure 6).

Interestingly, DBM occurrences in the antarctic regime are restricted to a limited sector south of Australia and south of the Polar Front (Figure 5). This challenges earlier suggestions of a circumpolar presence of high-latitude subsurface maxima, commonly reported in the Australian sector (Baldry et al., 2020; Parslow et al., 2001; Westwood et al., 2011), across the entire Polar Frontal Zone (Boyd et al., 2024). This spatial confinement may result from unique stratification conditions in this region. South of the Polar Front, stratification is both shallower and stronger compared to other parts of the sector, as shown by maps of the maximum vertical gradient in buoyancy frequency (N^2) within Cluster 4 (Figure 8). Such localized structure likely promotes the retention of a subsurface phytoplankton community (Uitz et al., 2009). This assemblage is probably dominated by diatoms (Baldry et al., 2020; Boyd et al., 2024), which might regulate their buoyancy to exploit recycled nutrients just below the MLD (Boyd et al., 2024). In contrast, in the rest of the Polar Frontal Zone, where stratification is weaker and/or deeper, enhanced vertical mixing and reduced light may prevent phytoplankton growth at depth.

Beyond their detection as vertical structures, DCM/DBM features can substantially reshape where productivity is located in the water column. Recent BGC-Argo-based estimates of primary production in the Southern Ocean (Vives et al., 2025) show that when a DBM is present, subsurface production (below the MLD) can represent a major fraction of column-integrated primary production (~60%), compared to ~17% on average. This highlights that surface observations alone may miss not only a substantial fraction of biomass (Figure S6 in Supporting Information S1), but also a potentially large share of production occurring below the mixed layer. Such a vertical decoupling between surface and subsurface signals may have implications for trophic coupling and carbon export (Baldry et al., 2020; Boyd et al., 2024).

4.3.2. Large-Scale Atmospheric Forcing

Winter MLD variability is significantly related to the SAM index in both the subtropical (Cluster 1) and antarctic (Cluster 4) regimes (Figure 7). A positive SAM phase is associated with a strengthening and poleward shift of the westerly winds (Thompson & Wallace, 2000), which in turn influences the MLD through changes in buoyancy and mechanical forcing (Sallée et al., 2010). Previous studies have shown that the relationship between SAM and MLD anomalies varies across different sectors of the Southern Ocean and with seasons (Buongiorno Nardelli et al., 2017). The contrasting relationships observed between subtropical and antarctic latitudes (Figure 7; e.g., Buongiorno Nardelli et al., 2017; Wang et al., 2022) may reflect the latitudinal redistribution of the westerly winds, which tend to weaken at lower latitudes and strengthen at higher latitudes during positive SAM phases, with the opposite pattern during negative phases. At subantarctic latitudes, north of the ACC, the asymmetric

influence of the SAM on the MLD (Buongiorno Nardelli et al., 2017; Sallée et al., 2010) may further explain the absence of a significant relationship in this regime.

In the subtropical regime (Cluster 1), where nitrate availability primarily limits primary production, interannual deepening of the winter MLD, significantly related to SAM variability, might enhance nutrient supply and increase phytoplankton biomass in spring. Conversely, during positive SAM phases, the maximum winter MLD tends to be shallower, which may reduce vertical nitrate supply to surface waters and limit phytoplankton growth (Figure 7). This interpretation is supported by the consistent annual winter mixing down to the nitracline in this region, where nitrate concentrations increase steeply with depth (Figure S9 in Supporting Information S1). These findings are also consistent with CMIP5 projections suggesting a future nutrient-driven decline in phytoplankton and export production across subtropical latitudes due to a reduction in winter mixing (Hauck et al., 2015). Finally, the SAM-biomass correlation was weaker than the SAM–MLD correlation in our analysis, consistent with an indirect SAM influence on biomass mediated by winter mixing.

In contrast, in antarctic regimes where primary production is predominantly limited by iron and light, interannual variations in phytoplankton biomass were not linked to interannual variability in winter MLD potentially driven by the SAM. The absence of correlation between phytoplankton biomass and maximum winter MLD is likely to reflect the already deep winter MLDs in the region, where further deepening would have limited effect on iron entrainment and may instead exacerbate light limitation on phytoplankton growth (Ardyna et al., 2017; Llort et al., 2015). Additionally, if the iron reservoir lies much deeper than the MLD could reach, the modest year-to-year variations in MLD (by ∼22 m) are unlikely to significantly alter iron supply (Llort et al., 2019). These findings contrast with satellite-based (Lovenduski & Gruber, 2005) and model-based projections (Hauck et al., 2015) suggesting an increase in iron supply and productivity under the positive SAM phase. In our observation-based analysis, however, the interannual variability captured over 2002–2021 does not provide evidence for such a mechanistic link in the antarctic regimes.

5. Conclusions

Using a 25-year gridded product of weekly vertical profiles of Chl*a* and b_{bp}, this study provides a bioregionalization of Southern Ocean phytoplankton phenology (available on Zenodo: 10.5281/zenodo.18368422; Mayot, 2026). In contrast to earlier efforts (Ardyna et al., 2017; Fay & McKinley, 2014; Thomalla et al., 2011), our approach explicitly incorporates the vertical dimension of phytoplankton biomass, alongside its seasonal variability, and further evaluates the interannual variability of the obtained bioregionalization over the last two decades.

Six coherent bioregions emerge, organized primarily along a latitudinal gradient with three major regimes: subtropical, subantarctic, and antarctic. The latitudinal structure of these regimes is partly driven by the light availability gradient along the latitude (Ardyna et al., 2017; Simon et al., 2025). However, the exact location of the boundaries between these regimes appears to be shaped by iron availability and the Subantarctic Front, while localized iron inputs generate non-zonal structures within the antarctic regime. Each year, ∼43% of the Southern Ocean follows these expected phenological patterns, ∼21% shows interannual variability, ∼30% exhibits undefined phenological patterns, and ∼6% remains unclassified due to data gaps. This relatively large fraction of undefined phenology, especially at high latitudes, is consistent with earlier reports of pronounced non-seasonal variability in the Southern Ocean (Prend et al., 2022; Thomalla et al., 2011).

Our analysis further highlights regional contrasts in the processes shaping DCMs. In the antarctic regime, DCMs corresponding to DBMs are restricted to areas south of the Polar Front in the Australian sector, where favorable stratification may promote subsurface accumulation of diatoms. In contrast, in subtropical and subantarctic regions, photoacclimation contributes significantly to the formation of DCMs.

In the subtropical regime, interannual shoaling (deepening) of winter mixing, partly modulated by positive (negative) SAM phases, may reduce (enhance) spring phytoplankton biomass levels. These results align with climate projections of future nutrient-driven declines in subtropical productivity under reduced winter mixing (Hauck et al., 2015). In contrast, our findings do not confirm earlier satellite- and model-based studies (Hauck et al., 2015; Lovenduski & Gruber, 2005) that suggested enhanced antarctic productivity under positive SAM phases, nor do they corroborate decadal regime shifts over the last 20 years (Thomalla et al., 2023). The absence of long-term expansion or contraction of the identified six bioregions suggests that large-scale changes in frontal

positions or iron supply have been limited over the past two decades. Yet, this apparent stability does not preclude shifts in phytoplankton community composition (Hayward et al., 2025) or changes occurring outside our observational domain. Future efforts should aim to connect our phenological regimes with community structure and quantify their implications for primary production, carbon export, and air-to-sea CO_2 flux. Because our analysis is restricted to ice-free regions, we cannot exclude that longer-term trends and decadal variability are more pronounced in sea-ice influenced regions. Extending this bioregionalization framework based on vertical phytoplankton biomass profiles into the seasonal ice zone will therefore be an important next step as year-round high-latitude observations continue to expand, partly thanks to autonomous platforms capable of under-ice sampling (e.g., Polar Argo mission of the OneArgo program).

Conflict of Interest

The authors declare no conflicts of interest relevant to this study.

Availability Statement

This study was conducted using data from the E.U. Copernicus Marine Service Information, accessed in January 2025: a global four-dimensional Chl*a* and b_{bp} product (https://doi.org/10.48670/moi-00046) (Sauzède et al., 2024), and the ARMOR3D product (https://doi.org/10.48670/moi-00052) (Verbrugge et al., 2024). Python scripts used to perform the analyses and generate the figures presented in this study are archived on Zenodo (https://doi.org/10.5281/zenodo.18368422) (Mayot, 2026).

Acknowledgments
This research was supported by the CNES (Centre National d'Etudes Spatiales) thanks to a postdoctoral allowance granted to N.M. in 2025. N.M. acknowledges the Institut de l'Océan and the Institut des Sciences du Calcul et des Données (ISCD) of Sorbonne University Alliance (IDEX SUPER 11-IDEX-0004) for their support of the project-team FORMAL (From ObseRving to Modeling oceAn Life). J. U. acknowledges the support of the French government within the framework of the "Investissements d'avenir" program integrated in France 2030 and managed by the Agence Nationale de la Recherche (ANR) under the reference ANR-21-ESRE-0019 (project Argo-2030) and acknowledges the funding from the European Research Council (ERC) under the European Union's Horizon 2020 research and innovation program (Grant agreement N° 834177, project REFINE). Open access publication funding provided by COUPERIN CY26.

References

Ardyna, M., Claustre, H., Sallée, J.-B., D'Ovidio, F., Gentili, B., van Dijken, G., et al. (2017). Delineating environmental control of phytoplankton biomass and phenology in the Southern Ocean. *Geophysical Research Letters*, *44*(10), 5016–5024. https://doi.org/10.1002/2016GL072428

Ardyna, M., Lacour, L., Sergi, S., d'Ovidio, F., Sallée, J.-B., Rembauville, M., et al. (2019). Hydrothermal vents trigger massive phytoplankton blooms in the Southern Ocean. *Nature Communications*, *10*(1), 2451. https://doi.org/10.1038/s41467-019-09973-6

Argo (2025). Argo float data and metadata from Global Data Assembly Centre (Argo GDAC)—Snapshot of Argo GDAC of August 2024 [Dataset]. *SEANOE*. https://doi.org/10.17882/42182%2523107470

Baldry, K., Strutton, P. G., Hill, N. A., & Boyd, P. W. (2020). Subsurface Chlorophyll-*a* maxima in the Southern Ocean. *Frontiers in Marine Science*, *7*, 671. https://doi.org/10.3389/fmars.2020.00671

Barbieux, M., Uitz, J., Gentili, B., Pasqueron de Fommervault, O., Mignot, A., Poteau, A., et al. (2019). Bio-optical characterization of subsurface chlorophyll maxima in the Mediterranean Sea from a Biogeochemical-Argo float database. *Biogeosciences*, *16*(6), 1321–1342. https://doi.org/10.5194/bg-16-1321-2019

Barbieux, M., Uitz, J., Mignot, A., Roesler, C., Claustre, H., Gentili, B., et al. (2022). Biological production in two contrasted regions of the Mediterranean Sea during the oligotrophic period: An estimate based on the diel cycle of optical properties measured by BioGeoChemical-Argo profiling floats. *Biogeosciences*, *19*(4), 1165–1194. https://doi.org/10.5194/bg-19-1165-2022

Baudena, A., Riom, W., Taillandier, V., Mayot, N., Mignot, A., & D'Ortenzio, F. (2025). Comparing satellite and BGC-Argo chlorophyll estimation: A phenological study. *Remote Sensing of Environment*, *326*, 114743. https://doi.org/10.1016/j.rse.2025.114743

Behrenfeld, M. J. (2010). Abandoning Sverdrup's critical depth Hypothesis on phytoplankton blooms. *Ecology*, *91*(4), 977–989. https://doi.org/10.1890/09-1207.1

Bellacicco, M., Cornec, M., Organelli, E., Brewin, R. J. W., Neukermans, G., Volpe, G., et al. (2019). Global variability of optical backscattering by non-algal particles from a biogeochemical-argo data set. *Geophysical Research Letters*, *46*(16), 9767–9776. https://doi.org/10.1029/2019GL084078

Bittig, H. C., Maurer, T. L., Plant, J. N., Schmechtig, C., Wong, A. P. S., Claustre, H., et al. (2019). A BGC-argo guide: Planning, deployment, data handling and usage. *Frontiers in Marine Science*, *6*, 502. https://doi.org/10.3389/fmars.2019.00502

Blain, S., Quéguiner, B., Armand, L., Belviso, S., Bombled, B., Bopp, L., et al. (2007). Effect of natural iron fertilization on carbon sequestration in the Southern Ocean. *Nature*, *446*(7139), 1070–1074. https://doi.org/10.1038/nature05700

Bock, N., Cornec, M., Claustre, H., & Duhamel, S. (2022). Biogeographical classification of the Global Ocean from BGC-Argo floats. *Global Biogeochemical Cycles*, *36*(6), e2021GB007233. https://doi.org/10.1029/2021GB007233

Boss, E., & Behrenfeld, M. (2010). In situ evaluation of the initiation of the North Atlantic phytoplankton bloom. *Geophysical Research Letters*, *37*(18). https://doi.org/10.1029/2010GL044174

Boss, E., Picheral, M., Leeuw, T., Chase, A., Karsenti, E., Gorsky, G., et al. (2013). The characteristics of particulate absorption, scattering and attenuation coefficients in the surface ocean; contribution of the Tara Oceans expedition. *Methods in Oceanography*, *7*, 52–62. https://doi.org/10.1016/j.mio.2013.11.002

Boyd, P. W. (2002). Environmental factors controlling phytoplankton processes in the Southern Ocean. *Journal of Phycology*, *38*(5), 844–861. https://doi.org/10.1046/j.1529-8817.2002.t01-1-01203.x

Boyd, P. W., Antoine, D., Baldry, K., Cornec, M., Ellwood, M., Halfter, S., et al. (2024). Controls on polar Southern Ocean deep chlorophyll maxima: Viewpoints from multiple observational platforms. *Global Biogeochemical Cycles*, *38*(3), e2023GB008033. https://doi.org/10.1029/2023GB008033

Boyd, P. W., Arrigo, K. R., Strzepek, R., & van Dijken, G. L. (2012). Mapping phytoplankton iron utilization: Insights into Southern Ocean supply mechanisms. *Journal of Geophysical Research*, *117*(C6). https://doi.org/10.1029/2011JC007726

Buongiorno Nardelli, B., Guinehut, S., Verbrugge, N., Cotroneo, Y., Zambianchi, E., & Iudicone, D. (2017). Southern Ocean mixed-layer seasonal and interannual variations from combined satellite and in situ data. *Journal of Geophysical Research: Oceans*, *122*(12), 10042–10060. https://doi.org/10.1002/2017JC013314

Carranza, M. M., Gille, S. T., Franks, P. J. S., Johnson, K. S., Pinkel, R., & Girton, J. B. (2018). When mixed layers are not mixed. Storm-driven mixing and bio-optical vertical gradients in mixed layers of the Southern Ocean. *Journal of Geophysical Research: Oceans*, *123*(10), 7264–7289. https://doi.org/10.1029/2018JC014416

Cassar, N., Bender, M. L., Barnett, B. A., Fan, S., Moxim, W. J., Levy, H., & Tilbrook, B. (2007). The Southern Ocean biological response to aeolian iron deposition. *Science*, *317*(5841), 1067–1070. https://doi.org/10.1126/science.1144602

Chapman, C. C. (2017). New perspectives on frontal variability in the Southern Ocean. https://doi.org/10.1175/JPO-D-16-0222.1

Chapman, C. C., Lea, M.-A., Meyer, A., Sallée, J.-B., & Hindell, M. (2020). Defining Southern Ocean fronts and their influence on biological and physical processes in a changing climate. *Nature Climate Change*, *10*(3), 209–219. https://doi.org/10.1038/s41558-020-0705-4

Cornec, M., Claustre, H., Mignot, A., Guidi, L., Lacour, L., Poteau, A., et al. (2021). Deep chlorophyll maxima in the global ocean: Occurrences, drivers and characteristics. *Global Biogeochemical Cycles*, *35*(4), e2020GB006759. https://doi.org/10.1029/2020GB006759

Cullen, J. J. (2015). Subsurface chlorophyll maximum layers: Enduring enigma or mystery solved? *Annual Review of Marine Science*, *7*(1), 207–239. https://doi.org/10.1146/annurev-marine-010213-135111

Del Castillo, C. E., Signorini, S. R., Karaköylü, E. M., & Rivero-Calle, S. (2019). Is the Southern Ocean getting greener? *Geophysical Research Letters*, *46*(11), 6034–6040. https://doi.org/10.1029/2019GL083163

d'Ovidio, F., Della Penna, A., Trull, T. W., Nencioli, F., Pujol, M.-I., Rio, M.-H., et al. (2015). The biogeochemical structuring role of horizontal stirring: Lagrangian perspectives on iron delivery downstream of the Kerguelen Plateau. *Biogeosciences*, *12*(19), 5567–5581. https://doi.org/10.5194/bg-12-5567-2015

Eayrs, C., Li, X., Raphael, M. N., & Holland, D. M. (2021). Rapid decline in Antarctic sea ice in recent years hints at future change. *Nature Geoscience*, *14*(7), 460–464. https://doi.org/10.1038/s41561-021-00768-3

Fauchereau, N., Tagliabue, A., Bopp, L., & Monteiro, P. M. S. (2011). The response of phytoplankton biomass to transient mixing events in the Southern Ocean. *Geophysical Research Letters*, *38*(17). https://doi.org/10.1029/2011GL048498

Fay, A. R., & McKinley, G. A. (2014). Global open-ocean biomes: Mean and temporal variability. *Earth System Science Data*, *6*(2), 273–284. https://doi.org/10.5194/essd-6-273-2014

Fennel, K., & Boss, E. (2003). Subsurface maxima of phytoplankton and chlorophyll: Steady-state solutions from a simple model. *Limnology & Oceanography*, *48*(4), 1521–1534. https://doi.org/10.4319/lo.2003.48.4.1521

Fonvieille, N., Guinet, C., Saraceno, M., Picard, B., Tournier, M., Goulet, P., et al. (2023). Swimming in an ocean of curves: A functional approach to understanding elephant seal habitat use in the Argentine Basin. *Progress in Oceanography*, *218*, 103120. https://doi.org/10.1016/j.pocean.2023.103120

Friedlingstein, P., O'Sullivan, M., Jones, M. W., Andrew, R. M., Hauck, J., Landschützer, P., et al. (2025). Global Carbon Budget 2024. *Earth System Science Data*, *17*(3), 965–1039. https://doi.org/10.5194/essd-17-965-2025

Garcia, H. E., Bouchard, C., Cross, S. L., Paver, C. R., Reagan, J. R., Boyer, T. P., et al. (2024). World Ocean Atlas 2023, volume 4: Dissolved inorganic nutrients (phosphate, nitrate, and silicate). https://doi.org/10.25923/39qw-7j08

Golder, M. R., & Antoine, D. (2025). Physical drivers of long-term chlorophyll-*a* variability in the Southern Ocean. *Elementa: Science of the Anthropocene*, *13*(1), 00077. https://doi.org/10.1525/elementa.2024.00077

Gong, D., & Wang, S. (1999). Definition of Antarctic Oscillation index. *Geophysical Research Letters*, *26*(4), 459–462. https://doi.org/10.1029/1999GL900003

Graff, J. R., Westberry, T. K., Milligan, A. J., Brown, M. B., Dall'Olmo, G., Dongen-Vogels, V. V., et al. (2015). Analytical phytoplankton carbon measurements spanning diverse ecosystems. *Deep Sea Research Part I: Oceanographic Research Papers*, *102*, 16–25. https://doi.org/10.1016/j.dsr.2015.04.006

Graham, R. M., De Boer, A. M., van Sebille, E., Kohfeld, K. E., & Schlosser, C. (2015). Inferring source regions and supply mechanisms of iron in the Southern Ocean from satellite chlorophyll data. *Deep Sea Research Part I: Oceanographic Research Papers*, *104*, 9–25. https://doi.org/10.1016/j.dsr.2015.05.007

Gregor, L., Kok, S., & Monteiro, P. M. S. (2018). Interannual drivers of the seasonal cycle of CO_2 in the Southern Ocean. *Biogeosciences*, *15*(8), 2361–2378. https://doi.org/10.5194/bg-15-2361-2018

Gruber, N., Landschützer, P., & Lovenduski, N. S. (2019). The variable Southern Ocean carbon sink. *Annual Review of Marine Science*, *11*(1), 159–186. https://doi.org/10.1146/annurev-marine-121916-063407

Guinehut, S., Dhomps, A.-L., Larnicol, G., & Le Traon, P.-Y. (2012). High resolution 3-D temperature and salinity fields derived from in situ and satellite observations. *Ocean Science*, *8*(5), 845–857. https://doi.org/10.5194/os-8-845-2012

Hardman-Mountford, N. J., Hirata, T., Richardson, K. A., & Aiken, J. (2008). An objective methodology for the classification of ecological pattern into biomes and provinces for the pelagic ocean. *Remote Sensing of Environment*, *112*(8), 3341–3352. https://doi.org/10.1016/j.rse.2008.02.016

Hauck, J., Gregor, L., Nissen, C., Patara, L., Hague, M., Mongwe, P., et al. (2023). The Southern Ocean carbon cycle 1985–2018: Mean, seasonal cycle, trends, and storage. *Global Biogeochemical Cycles*, *37*(11), e2023GB007848. https://doi.org/10.1029/2023GB007848

Hauck, J., Völker, C., Wolf-Gladrow, D. A., Laufkötter, C., Vogt, M., Aumont, O., et al. (2015). On the Southern Ocean CO_2 uptake and the role of the biological carbon pump in the 21st century. *Global Biogeochemical Cycles*, *29*(9), 1451–1470. https://doi.org/10.1002/2015GB005140

Hayward, A., Wright, S. W., Carroll, D., Law, C. S., Wongpan, P., Gutiérrez-Rodriguez, A., & Pinkerton, M. H. (2025). Antarctic phytoplankton communities restructure under shifting sea-ice regimes. *Nature Climate Change*, *15*, 1–8. https://doi.org/10.1038/s41558-025-02379-x

Hermilly, T., Martinez, E., Uitz, J., Cornec, M., Kolodziejczyk, N., & Schmechtig, C. (2025). Seasonal variability of phytoplankton vertical distribution in a contrasted South Pacific Ocean from BioGeoChemical-Argo profiling floats. *Geophysical Research Letters*, *52*(18), e2024GL114262. https://doi.org/10.1029/2024GL114262

Hunt, G. L., Drinkwater, K. F., Arrigo, K., Berge, J., Daly, K. L., Danielson, S., et al. (2016). Advection in polar and sub-polar environments: Impacts on high latitude marine ecosystems. *Progress in Oceanography*, *149*, 40–81. https://doi.org/10.1016/j.pocean.2016.10.004

Jones, D. C., Holt, H. J., Meijers, A. J. S., & Shuckburgh, E. (2019). Unsupervised clustering of Southern Ocean argo float temperature profiles. *Journal of Geophysical Research: Oceans*, *124*(1), 390–402. https://doi.org/10.1029/2018JC014629

Kuhn, A. M., Mazloff, M. R., Gille, S. T., & Verdy, A. (2025). Sensitivity of chlorophyll vertical structure to model parameters in the biogeochemical Southern Ocean state estimate (B-SOSE). *Journal of Geophysical Research: Biogeosciences*, *130*(1), e2024JG008300. https://doi.org/10.1029/2024JG008300

Lacour, L., Briggs, N., Claustre, H., Ardyna, M., & Dall'Olmo, G. (2019). The intraseasonal dynamics of the mixed layer pump in the subpolar North Atlantic Ocean: A biogeochemical-argo float approach. *Global Biogeochemical Cycles*, *33*(3), 266–281. https://doi.org/10.1029/2018GB005997

Lacour, L., Llort, J., Briggs, N., Strutton, P. G., & Boyd, P. W. (2023). Seasonality of downward carbon export in the Pacific Southern Ocean revealed by multi-year robotic observations. *Nature Communications*, *14*(1), 1278. https://doi.org/10.1038/s41467-023-36954-7

Lannuzel, D., Schoemann, V., de Jong, J., Pasquer, B., van der Merwe, P., Masson, F., et al. (2010). Distribution of dissolved iron in Antarctic sea ice: Spatial, seasonal, and inter-annual variability. *Journal of Geophysical Research*, *115*(G3). https://doi.org/10.1029/2009JG001031

Liniger, G., Sharp, J. D., Takeshita, Y., & Johnson, K. S. (2025). Two decades of increase in Southern Ocean net community production revealed by BGC-argo floats. *Global Biogeochemical Cycles*, *39*(8), e2024GB008371. https://doi.org/10.1029/2024GB008371

Llort, J., Lévy, M., Sallée, J.-B., & Tagliabue, A. (2015). Onset, intensification, and decline of phytoplankton blooms in the Southern Ocean. *ICES Journal of Marine Science*, *72*(6), 1971–1984. https://doi.org/10.1093/icesjms/fsv053

Llort, J., Lévy, M., Sallée, J. B., & Tagliabue, A. (2019). Nonmonotonic response of primary production and export to changes in mixed-layer depth in the Southern Ocean. *Geophysical Research Letters*, *46*(6), 3368–3377. https://doi.org/10.1029/2018GL081788

Loisel, H., Nicolas, J.-M., Deschamps, P.-Y., & Frouin, R. (2002). Seasonal and inter-annual variability of particulate organic matter in the global ocean. *Geophysical Research Letters*, *29*(24), 49-1-49–4. https://doi.org/10.1029/2002GL015948

Longhurst, A. R. (2007a). Chapter 5—Nutrient limitation: The example of iron. In A. R. Longhurst (Ed.), *Ecological geography of the sea* (2nd ed., pp. 71–87). Academic Press. https://doi.org/10.1016/B978-012455521-1/50006-1

Longhurst, A. R. (2007b). Chapter 12—The Southern Ocean. In A. R. Longhurst (Ed.), *Ecological geography of the Sea* (2nd ed., pp. 443–475). Academic Press. https://doi.org/10.1016/B978-012455521-1/50013-9

Lovenduski, N. S., & Gruber, N. (2005). Impact of the Southern Annular Mode on Southern Ocean circulation and biology. *Geophysical Research Letters*, *32*(11). https://doi.org/10.1029/2005GL022727

Marshall, G. J. (2003). Trends in the Southern annular mode from observations and reanalyses. *Journal of Climate*, *16*(24), 4134–4143. https://doi.org/10.1175/1520-0442(2003)016<4134:titsam>2.0.co;2

Mayot, N. (2026). Bioregionalization of the Southern Ocean based on phytoplankton biomass distribution: Datasets and Python Code [Dataset]. *Zenodo*. https://doi.org/10.5281/zenodo.18368422

Mayot, N., Le Quéré, C., Rödenbeck, C., Bernardello, R., Bopp, L., Djeutchouang, L. M., et al. (2023). Climate-driven variability of the Southern Ocean CO_2 sink. *Philosophical Transactions of the Royal Society A: Mathematical, Physical and Engineering Sciences*, *381*(2249), 20220055. https://doi.org/10.1098/rsta.2022.0055

Mignot, A., Claustre, H., Uitz, J., Poteau, A., D'Ortenzio, F., & Xing, X. (2014). Understanding the seasonal dynamics of phytoplankton biomass and the deep chlorophyll maximum in oligotrophic environments: A Bio-Argo float investigation. *Global Biogeochemical Cycles*, *28*(8), 856–876. https://doi.org/10.1002/2013GB004781

Mongwe, N. P., Gregor, L., Tjiputra, J., Hauck, J., Ito, T., Danek, C., et al. (2024). Projected poleward migration of the Southern Ocean CO_2 sink region under high emissions. *Communications Earth & Environment*, *5*(1), 1–13. https://doi.org/10.1038/s43247-024-01382-y

Mulet, S., Rio, M.-H., Mignot, A., Guinehut, S., & Morrow, R. (2012). A new estimate of the global 3D geostrophic ocean circulation based on satellite data and in-situ measurements. *Deep Sea Research Part II: Topical Studies in Oceanography*, *77–80*, 70–81. https://doi.org/10.1016/j.dsr2.2012.04.012

Park, Y. H., & Durand, I. (2019). Altimetry-drived Antarctic Circumpolar current fronts [Dataset]. *SEANOE*. https://doi.org/10.17882/59800

Park, Y. H., Park, T., Kim, T.-W., Lee, S.-H., Hong, C.-S., Lee, J.-H., et al. (2019). Observations of the Antarctic circumpolar current over the udintsev fracture zone, the narrowest Choke point in the Southern Ocean. *Journal of Geophysical Research: Oceans*, *124*(7), 4511–4528. https://doi.org/10.1029/2019JC015024

Parslow, J. S., Boyd, P. W., Rintoul, S. R., & Griffiths, F. B. (2001). A persistent subsurface chlorophyll maximum in the Interpolar Frontal Zone south of Australia: Seasonal progression and implications for phytoplankton-light-nutrient interactions. *Journal of Geophysical Research*, *106*(C12), 31543–31557. https://doi.org/10.1029/2000JC000322

Prend, C. J., Keerthi, M. G., Lévy, M., Aumont, O., Gille, S. T., & Talley, L. D. (2022). Sub-seasonal forcing drives year-to-year variations of Southern Ocean primary productivity. *Global Biogeochemical Cycles*, *36*(7), e2022GB007329. https://doi.org/10.1029/2022GB007329

Reygondeau, G., Longhurst, A., Martinez, E., Beaugrand, G., Antoine, D., & Maury, O. (2013). Dynamic biogeochemical provinces in the global ocean. *Global Biogeochemical Cycles*, *27*(4), 1046–1058. https://doi.org/10.1002/gbc.20089

Rintz, C. L., Koubbi, P., Ramiro-Sánchez, B., Azarian, C., Caccavo, J. A., Cotté, C., et al. (2025). Biogeographical regions and climate change: Lanternfishes shed light on the role of climatic barriers in the Southern Ocean. *Global Change Biology*, *31*(6), e70256. https://doi.org/10.1111/gcb.70256

Sallée, J. B., Llort, J., Tagliabue, A., & Lévy, M. (2015). Characterization of distinct bloom phenology regimes in the Southern Ocean. *ICES Journal of Marine Science*, *72*(6), 1985–1998. https://doi.org/10.1093/icesjms/fsv069

Sallée, J. B., Speer, K. G., & Rintoul, S. R. (2010). Zonally asymmetric response of the Southern Ocean mixed-layer depth to the Southern Annular Mode. *Nature Geoscience*, *3*(4), 273–279. https://doi.org/10.1038/ngeo812

Sarmiento, J. L., Johnson, K. S., Arteaga, L. A., Bushinsky, S. M., Cullen, H. M., Gray, A. R., et al. (2023). The Southern Ocean carbon and climate observations and modeling (SOCCOM) project: A review. *Progress in Oceanography*, *219*, 103130. https://doi.org/10.1016/j.pocean.2023.103130

Sauzède, R., Claustre, H., Uitz, J., Jamet, C., Dall'Olmo, G., D'Ortenzio, F., et al. (2016). A neural network-based method for merging ocean color and Argo data to extend surface bio-optical properties to depth: Retrieval of the particulate backscattering coefficient. *Journal of Geophysical Research: Oceans*, *121*(4), 2552–2571. https://doi.org/10.1002/2015JC011408

Sauzède, R., Renosh, P. R., Schmechtig, C., Uitz, J., & Claustre, H. (2024). Global Ocean 3D Chlorophyll-*a* concentration, Particulate Backscattering coefficient and Particulate Organic Carbon [Dataset]. *E.U Copernicus Marine Service Information (CMEMS): Marine Data Store (MDS)*. https://doi.org/10.48670/moi-00046

Schmechtig, C., Sauzède, R., Lemasson, P., Bretagnon, M., Renosh, P. R., & Claustre, H. (2025). Collection of BGC-Argo single synthetic profile files with improved post processed Chlorophyll-*a* at the global scale [Dataset]. *SEANOE*. https://doi.org/10.17882/102324

Simon, E., Lacour, L., Claustre, H., Bock, N., Cornec, M., Sauzède, R., et al. (2025). Linking surface phytoplankton dynamics to small-particle fluxes in the mesopelagic Zone: Insights from high latitude bioregions using BGC-Argo floats. *Global Biogeochemical Cycles*, *39*(7), e2024GB008447. https://doi.org/10.1029/2024GB008447

Stoer, A. C., & Fennel, K. (2024). Carbon-centric dynamics of Earth's marine phytoplankton. *Proceedings of the National Academy of Sciences*, *121*(45), e2405354121. https://doi.org/10.1073/pnas.2405354121

Stramski, D., & Kiefer, D. A. (1991). Light scattering by microorganisms in the open ocean. *Progress in Oceanography*, *28*(4), 343–383. https://doi.org/10.1016/0079-6611(91)90032-H

Sullivan, C. W., Arrigo, K. R., McClain, C. R., Comiso, J. C., & Firestone, J. (1993). Distributions of Phytoplankton blooms in the Southern Ocean. *Science*, *262*(5141), 1832–1837. https://doi.org/10.1126/science.262.5141.1832

Tagliabue, A., Kwiatkowski, L., Bopp, L., Butenschön, M., Cheung, W., Lengaigne, M., & Vialard, J. (2021). Persistent uncertainties in ocean net primary production climate change projections at regional scales raise challenges for assessing impacts on ecosystem services. *Frontiers in Climate*, *3*, 738224. https://doi.org/10.3389/fclim.2021.738224

Tagliabue, A., Sallée, J.-B., Bowie, A. R., Lévy, M., Swart, S., & Boyd, P. W. (2014). Surface-water iron supplies in the Southern Ocean sustained by deep winter mixing. *Nature Geoscience*, *7*(4), 314–320. https://doi.org/10.1038/ngeo2101

Thomalla, S. J., Fauchereau, N., Swart, S., & Monteiro, P. M. S. (2011). Regional scale characteristics of the seasonal cycle of chlorophyll in the Southern Ocean. *Biogeosciences*, *8*(10), 2849–2866. https://doi.org/10.5194/bg-8-2849-2011

Thomalla, S. J., Nicholson, S. A., Ryan-Keogh, T. J., & Smith, M. E. S. (2023). Widespread changes in Southern Ocean phytoplankton blooms linked to climate drivers. *Nature Climate Change*, *13*(9), 975–984. https://doi.org/10.1038/s41558-023-01768-4

Thomas, S. D. A., Jones, D. C., Faul, A., Mackie, E., & Pauthenet, E. (2021). Defining Southern Ocean fronts using unsupervised classification. *Ocean Science*, *17*(6), 1545–1562. https://doi.org/10.5194/os-17-1545-2021

Thompson, D. W. J., & Wallace, J. M. (2000). Annular modes in the extratropical circulation. Part I: Month-to-month variability. *Journal of Climate*, *13*(5), 1000–1016. https://doi.org/10.1175/1520-0442(2000)013<1000:amitec>2.0.co;2

Uchida, T., Balwada, D., Abernathey, R., Prend, C. J., Boss, E., & Gille, S. T. (2019). Southern Ocean phytoplankton blooms observed by biogeochemical floats. *Journal of Geophysical Research: Oceans*, *124*(11), 7328–7343. https://doi.org/10.1029/2019JC015355

Uitz, J., Claustre, H., Griffiths, F. B., Ras, J., Garcia, N., & Sandroni, V. (2009). A phytoplankton class-specific primary production model applied to the Kerguelen Islands region (Southern Ocean). *Deep Sea Research Part I: Oceanographic Research Papers*, *56*(4), 541–560. https://doi.org/10.1016/j.dsr.2008.11.006

Verbrugge, N., Greiner, E., & Zunino, P. (2024). Multi observation Global Ocean 3D temperature salinity height geostrophic Current and MLD [Dataset]. *E.U Copernicus Marine Service Information (CMEMS): Marine Data Store (MDS)*. https://doi.org/10.48670/moi-00052

Vives, C. R., Schallenberg, C., Strutton, P. G., Bendtsen, J., Richardson, K., & Boyd, P. W. (2025). The contribution of deep chlorophyll maxima to net primary production in the Southern Ocean. *Global Biogeochemical Cycles*, *39*(10), e2024GB008327. https://doi.org/10.1029/2024GB008327

Vives, C. R., Schallenberg, C., Strutton, P. G., & Boyd, P. W. (2024). Biogeochemical-Argo floats show that chlorophyll increases before carbon in the high-latitude Southern Ocean spring bloom. *Limnology and Oceanography Letters*, *9*(3), 172–182. https://doi.org/10.1002/lol2.10322

Wang, R., Nan, F., Yu, F., & Wang, B. (2022). Subantarctic mode water variations in the three Southern hemisphere Ocean basins during 2004–2019. *Journal of Geophysical Research: Oceans*, *127*(7), e2021JC017906. https://doi.org/10.1029/2021JC017906

Weis, J., Chase, Z., Schallenberg, C., Strutton, P. G., Bowie, A. R., & Fiddes, S. L. (2024). One-third of Southern Ocean productivity is supported by dust deposition. *Nature*, *629*(8012), 603–608. https://doi.org/10.1038/s41586-024-07366-4

Westwood, K. J., Brian Griffiths, F., Webb, J. P., & Wright, S. W. (2011). Primary production in the Sub-Antarctic and Polar Frontal zones south of Tasmania, Australia; SAZ-Sense survey, 2007. *Deep Sea Research Part II: Topical Studies in Oceanography*, *58*(21), 2162–2178. https://doi.org/10.1016/j.dsr2.2011.05.017